Atomic Structure of Defects and Dopants in 2D Layered Transition Metal Dichalcogenides

Shanshan Wang[1], Alex Robertson[2], Jamie H. Warner[2]

[1]Science and Technology on Advanced Ceramic Fibers and Composites Laboratory, National University of Defence Technology, Changsha 410073, PR China

[2]Department of Materials, University of Oxford, OX1 3PH, UK

Email: Jamie.warner@materials.ox.ac.uk

Abstract

Layered transition metal dichalcogenides (TMDs) offer monolayer 2D systems with diverse properties that extend beyond what graphene alone can achieve. The properties of TMDs are heavily influenced by the atomic structure and in particular imperfects in the crystallinity in the form of vacancy defects, grain boundaries, cracks, impurity dopants, ripples and edge terminations. This review will cover the current knowledge of the detailed structural forms of some of the most intensively studied 2D TMDs, such as MoS_2, WSe_2, MoTe, WTe, NbSe, PtSe, and also covers MXene. The review will utilize results achieved using state-of-the-art aberration corrected transmission electron microscopy, including annular dark-field scanning transmission electron microscopy (ADF-STEM) and electron energy loss spectroscopy (EELS), showing how elemental discrimination can be achieved to understand structure at a deep level. The review will also cover the impact of single atom substitutional dopants, such as Cr, V and Mn, and electron energy loss spectroscopy used to understand the local bonding configuration. It is expected that this review will provide an atomic level understanding of 2D TMDs with a connection to imperfections that can arise from

chemical vapour deposition synthesis, intentional doping, rips and tears, dislocations, strain, polycrystallinity and confinement to nanoribbons.

INTRODUCTION

2D materials have expanded dramatically since the first reports of graphene isolation, with the realization of semiconductors and insulators.[1–4] This has enabled measurements of photoluminescence from monolayer crystals and also the formation of light emitting devices and photodetectors in the visible spectral range. The main surge in semiconducting monolayers has been through the research into transition metal dichalcogenides, primarily with Mo and W metals, and Se, S and Te chalcogenides. Take monolayer MoS_2 as an example, the most commonly encountered polymorphs are 1H and 1T, having trigonal prismatic coordination (D_{3h} point group) and octahedral coordination (D_{3d}), respectively. The former one is more stable than the latter, with a lattice constant of ～3.2Å and a Mo-S bond length of ～2.4Å.[5–7] More importantly, in monolayer 1H form these TMDs are direct band gap semiconductors mostly in the red spectral region (MoS_2: ～1.9 eV, WS_2: ～2.0 eV) and in bulk they are indirect band gap materials.[8,9] This high sensitivity on band gap change with layer number makes it important to understand the monolayer form and also how the monolayers stack into bilayers, trilayers and beyond.[10–20] Further interest in TMDs has been generated by the valley spin splitting arising from spin-orbit coupling and this leads to well separated excitons for each valley state.[21] This extra spin degree of freedom has opened opportunities in valleytronics and also addressable spin states by optical spectroscopy at room temperature.[22,23] Even in monolayer form, the properties of TMDs can be altered by shifts in the chalcogenide positions from 1H to 1T phases that has profound impact on band gap and catalytic behaviour.[24,25] The ability to produce stacks of TMDs with alternating elemental composition, such as MoS_2:WS_2, provides rich heterostructure alignments, forming type II offsets that have rapid charge transfer, ideal for photodetectors and solar cells.[26–31]

A key aspect to the development of TMDs for future applications has been the ability to grow large area materials by chemical vapour deposition, leading to control of alloying to create Mo:W:Se:S blends, and also lateral interfaces between different TMDs.[32–35] The growth of TMDs by CVD evolves through the nucleation of small domains that then merge together as they grow into a larger polycrystalline film. This inevitably leads to grain boundaries between each seed nuclei. Control over growth can also be used to create bilayer TMD films with different TMD materials and also the incorporation of single dopant elements into the lattice as either substitutions or interstitials. Post addition of dopants to TMDs is also possible, generating surface bound species that are important for catalysis.[36]

Knowledge of the atomic structure of TMDs is crucial for proving the formation of these more complex alloys, but also to know the basic stacking structures and detailed arrangements of chalcogenide atoms. One of the leading methods to visualize atomic structure in 2D materials is aberration corrected transmission electron microscopy (AC-TEM).[37–44] The ultrathin nature of 2D materials makes them susceptible to electron beam induced damage by knock-on sputtering, which requires AC-TEM to be performed at low accelerating voltages of <80kV. However, even when using electron beam energies below the knock-on damage threshold, 2D materials still suffer atomic loss from the electron beam irradiation due to more complex phenomena, such as chemical etching. The high energy electron beam is capable of ionizing gas molecules in the vacuum chamber that react with the surface of the 2D materials and cause atomic loss.[45,46] Furthermore, the presence of diffusing atoms across the surface of 2D materials leads to chemical reactions under the electron beam that can also cause atomic loss. Therefore, using electron microscopy to quantify vacancy defects that are intrinsic to the sample, rather than from electron beam irradiation, is extremely difficult and such results should be taken with caution.

The two main forms of imaging by AC-TEM are phase contrast high resolution TEM, which relies on parallel beam illumination of the sample and the interference between the transmitted beam and the

diffracted beams to cause contrast changes associated with the atomic structure. This approach captures the large area field of view of the sample region and therefore can be used to observe dynamics and also measure bond strain. The down side is that it is not possible to couple this with elemental spectroscopy such as electron energy loss spectroscopy at the atomic level, but rather nanoscale resolution. Scanning transmission electron microscopy (STEM) can provide atom-by-atom probing of 2D materials because it uses a focussed electron beam of ~1Å, which is raster scanned across the sample to generate an image. Annular dark field STEM (ADF-STEM) imaging is achieved by placing an annular detector to collect scattered electrons. High angle ADF-STEM (HAADF-STEM), has contrast that goes with Z^2 for strong elemental discrimination. Medium and low scattering angles can also be captured, giving rise to MAADF-STEM and LAADF-STEM, respectively, with contrast that has less than quadratic dependence on Z number. ADF-STEM has an angular dependent contrast sensitivity, that can vary typically between $\sim Z^{1-2}$.[47] The transmitted electrons can also be analysed for the energy loss to obtain atomic resolution elemental spectroscopy. This can yield information not only on the elemental type, but also on the oxidation state and bonding. The following sections will focus on how AC-TEM is used to probe the atomic structure of 2D layered TMDs of Mo:W:Se:S compositions, including monolayer structure, interlayer stacking sequences, vacancies, dislocations, dopants, grain boundaries, surface adsorbates and edge terminations. It also includes sections on newly emerging 2D materials such as NbSe, $MoTe_2$, PtSe, and MXene.

1.1 Monolayers of MoS_2 and WS_2

Transition metal dichalcogenides composed of Mo, W metal atoms and S, Se chalcogenides are typically found in 1H configuration for the monolayer, figure 1, but also have a higher energy 1T phase. Other more exotic structural forms can be constructed, but are rarely found in existence due to their high energy and instabilities. Unlike graphene, which is truly only one atom thick, TMDs are three atom thick, with the metal atom in the middle and chalcogenides top and bottom, adopting trigonal prismatic form, figure 1a-

b. The 1T phase is formed by one layer of S atoms sliding across to give split positions of the S locations relative to the metal atoms. In experimental work, this has been achieved by using Li intercalation materials that help to stabilize the 1T form.[48] In a phase contrast TEM image of MoS_2 or WS_2, the intensity from the metal and chalcogenides are roughly similar, making it difficult to always distinguish the chalcogenide from the metal in the hexagonal lattice pattern. However using ADF-STEM, due to the *Z*-sensitive contrast, it is possible to distinguish the metal and chalcogenide sites (figure 1c-e).[49]

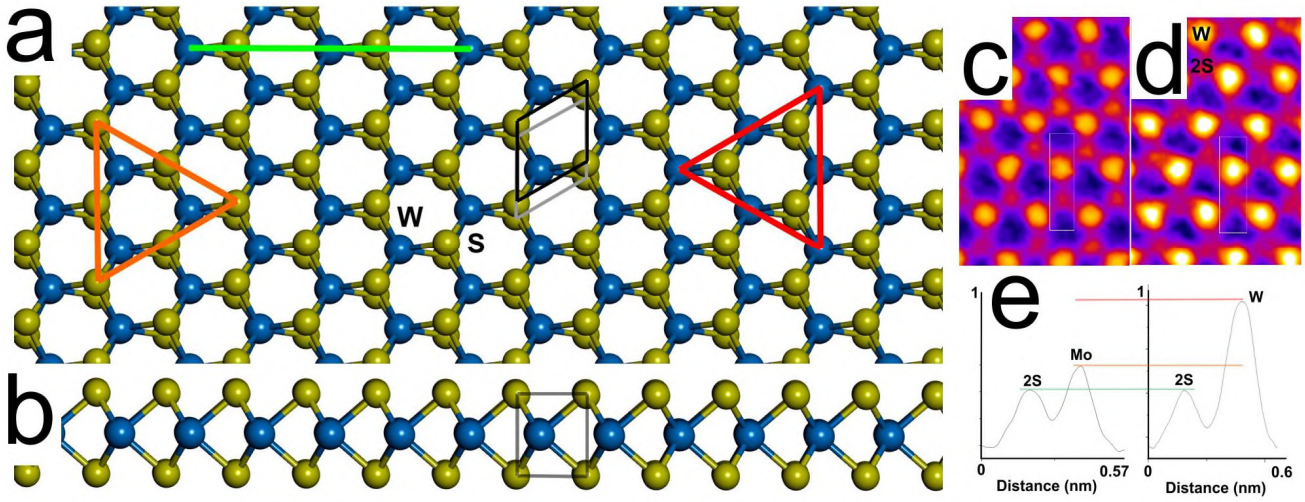

Figure 1. (a) Atomic model of monolayer WS_2 in 1H form with slight tilt to show both S atoms in each column, with green line indicating arm chair direction, orange triangle indicating S terminated zigzag directions and red triangle showing the Mo terminated zigzag directions. The unit cell is indicated by the black box. (c) and (d) show the ADF-STEM image of monolayer MoS_2 and WS_2 respectively. False 'fire' colour is used to highlight differences in Z number. (e) Line profiles taken from the white boxed areas in the respective images above, with normalization to the 2S intensity.

1.2 Bilayers of MoS_2 and WS_2

There are numerous possible interlayer stacking configurations that can be possible in TMDs, but the two most common and low energy stackings for MoS_2 and WS_2 are the 2H (AA') and the 3R (AB) types,

figure 2. The equilibrium interlayer distances for AA' and AB-stacked bilayer TMDs are very similar, being ~6.2 Å for MoS_2 and WS_2 and ~6.5Å for $MoSe_2$ and WSe_2, respectively. The small thickness variation between sulphides and selenides mainly originates from the difference size of S and Se atoms.[10] The energy difference between these two is small and therefore both are found in CVD grown materials.[50,51] Here we consider bilayer stackings, where AA' is produced by the 60° rotation of one layer with respect to the other, and the columns when view from above both have one metal and two chalcogenide atoms, figure 2h-m. This gives the same contrast for each column in an ADF-STEM image. For the AB stacked bilayer, both layers have the same lattice orientation, but one is translated slightly, figure 2a-g. This then gives three different columns when viewed from above, Mo+2S, Mo, and 2S, which in turn gives three contrast signals in an ADF-STEM image, figure 2b. This slight difference in contrast enables the 3R bilayer to be differentiated from the 1T phase of monolayer MoS_2, which has one Mo and 6 S atoms in projection.[49] In Se based TMDs, the 2Se atomic weight (68) is similar to the W metal atom (74) and this results in a more similar contrast from each column in the monolayer WS_2,[52] but also makes it harder to discriminate the 2H stacking from 1H layers. When misorientation of layers occurs, from rotational twists, then moiré patterns form, figure 2n, which can be across a wide range of angles and gives rise to complex contrast features. Moiré features are often produced when a monolayer back-folds on itself at an arbitrary angle.

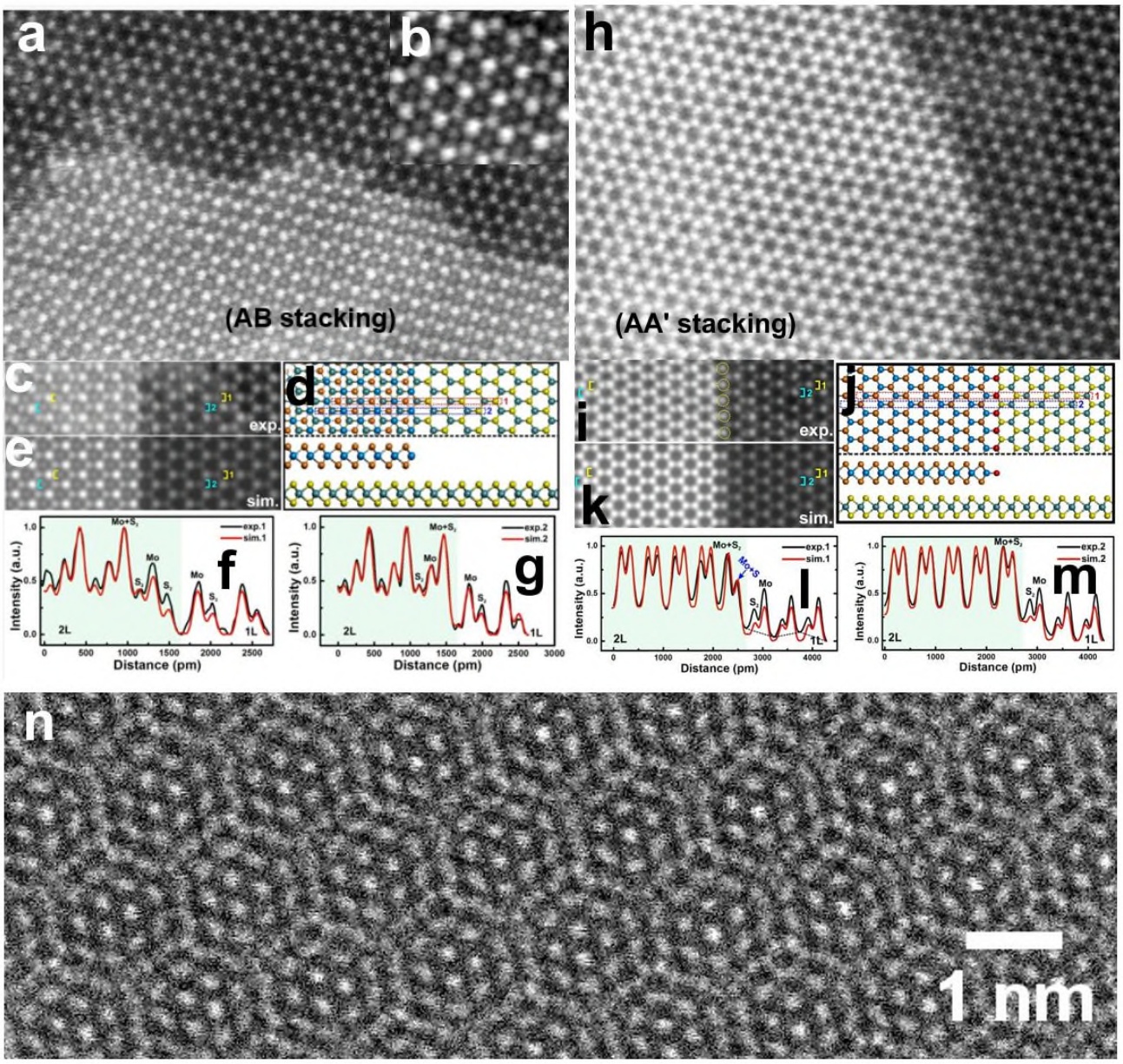

Figure 2. (a) ADF-STEM image of mono-bilayer MoS_2 interface with 3R (AB) stacking. (b) Higher magnification view of 3R stacked bilayer region. (c) ADF-STEM of the mono-bilayer interface for comparison with (d) atomic model and (e) multislice image simulation. (f) and (g) Line profile comparison for experiment and simulation from images (c) and (e). (h) ADF-STEM image of mono-bilayer MoS_2 interface with 2H (AB) stacking. (i) ADF-STEM of the mono-bilayer interface for comparison with (j) atomic model and (k) multislice image simulation. (l) and (m) Line profile comparison for experiment and

simulation from images (i) and (k). (n) ADF-STEM image of turbostratic stacked WS_2 bilayer showing moire pattern from 14° twist angle. (a)-(m) are reproduced with permission from ref. [50] © 2017 The Royal Society of Chemistry.

1.3 Bond rotations in WSe_2

Bond rotations are ubiquitous in graphene to form defects, even without loss of atoms.[53–55] They also help stabilize vacancies in graphene and are crucial in the dynamics of vacancy migration. However, in TMDs, bond rotation is much less prevalent due to the bi-element nature of the metal and chalcogenide bonding. Surprisingly, bond rotations have been observed in monolayer WSe_2 at elevated temperatures within vacancy clusters known as trefoil defects.[56] Figure 3(a)-(c) shows the series of ADF-STEM images whereby point Se vacancies aggregate and then transform into the trefoil defect with bond rotation. This leaves W metal atoms facing towards each other. Atomic models in figure 3(d)-(i) illustrate the mechanism of formation. Although this shows that bond rotations can exist in these bi-element 2D crystals, their wider observation across the range of TMD systems has been limited. To date, such defects have been only seen in WSe_2 and not in S based TMDs yet.

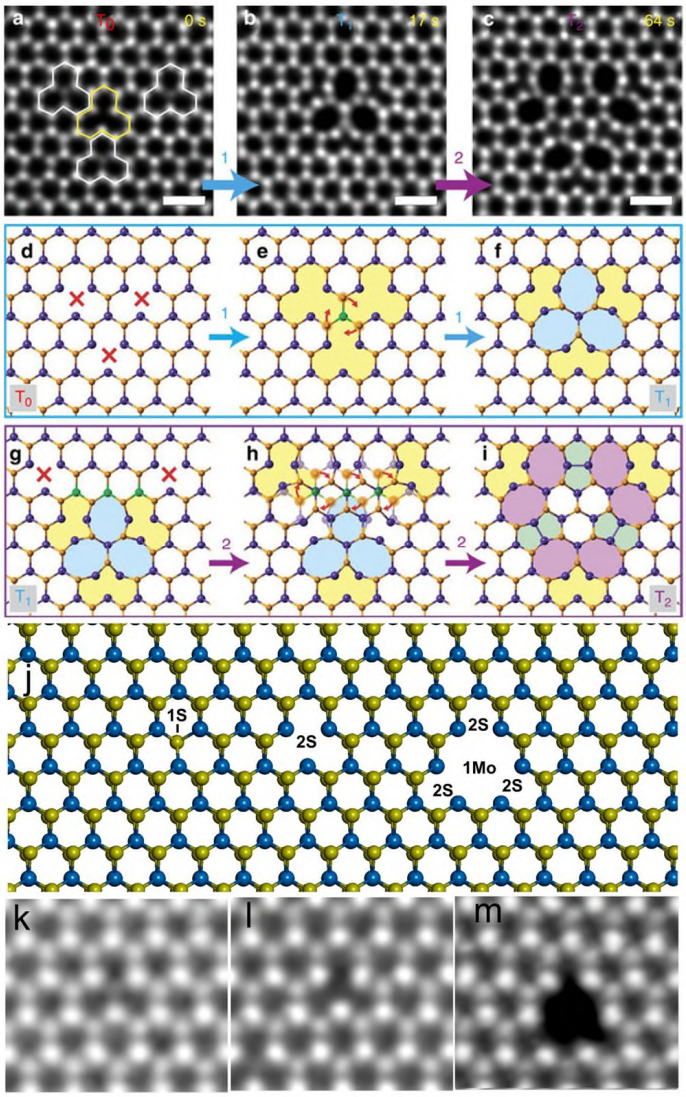

Figure 3. (a)-(c) Series of ADF-STEM images showing the formation of the trefoil defect in WSe_2. (d)-(i) Atomic models illustrating the mechanism of bond rotation in trefoil defect creation (j) Atomic model of monolayer MoS_2 showing the 1S, 2S, and 1Mo+2S(x3) vacancies. (k)-(m) ADF-STEM images of 1S, 2S and 1Mo+2S(x3) vacancies in monolayer MoS_2. (a)-(i) are reproduced with permission from ref. [56] © 2015 Macmillan Publishers Limited.

1.4 Vacancies in MoS_2

The most common form of vacancy in TMDs is the loss of a single chalcogenide atom, figure 3(j),(k). In MoS_2, S atomic loss is prevalent and can occur from both top and bottom layers. This loss of S atom can be detected in AC-TEM images by a reduced contrast, and more clearly in ADF-STEM images, figure 3(k).[57–59] Very little strain or bond reconstruction occurs around the 1S vacancy in TMDs.[60] The loss of two S atoms in the same column can also occur, but is less frequent, figure 3(l). This results in measurable bond contraction around the 2S vacancy core. During TEM imaging of TMDs, S atom loss occurs rapidly, with a knock-on threshold of ~6.5 eV, which is achievable with an electron accelerating voltage of 80kV.[46] However, S atom loss can occur at lower accelerating voltages (i.e 60kV) through more complex mechanisms, such as chemical etching effects and possibly ionization induced degradation.[45] 1S vacancies are mobile and diffuse within MoS_2 and aggregate into linear defect forms, figure 4a-c. These long line defects of S are aligned to the zigzag lattice direction of the MoS_2 and can increase in both length and width. As the length increases, the compression of lattice occurs within the central region of the line defect, due to the missing S atoms. Figure 4e,f show the displacement maps across a 1S line vacancy in MoS_2 monolayer for x (perpendicular) and y (parallel) to the line vacancy direction, showing compression in the x direction. As the width gets larger, the lattice distortions become evident and each Mo atom is only bonded to three S atoms, rather than 6 in the bulk, figure 4g,h. The S vacancy lines stagger top and bottom to stabilize the system and reduce buckling. The band structure also changes within these linear vacancies as a function of their width, gradually shifting from semiconducting to metallic. This means that large linear vacancy clusters can act as metallic channels within the semiconducting MoS_2 material and lead to complex transport behaviour.[61]

Because the S linear vacancy defects cause local compression strain around the central region, competing forces occur between linear defects along different zigzag angles. The trigonal symmetry of

monolayer 2H MoS_2 means that the strain from one linear defect is not completely orthogonal to the other linear vacancy defects. This results in the creation of inversion domains, as a means to accommodate local S depletion and the intersection of three linear vacancy lines to form triangular domains.[62] Inversion domains are so-called due to the swapping of the metal-chalcogenide lattice sites relative to the outside regions. These are commonly seen at high temperature, where S vacancy diffusion is thermally activated. In some cases a phase shift from 1H to 1T occurs within these triangular domains, triggered by the presence of metal dopants.[49]

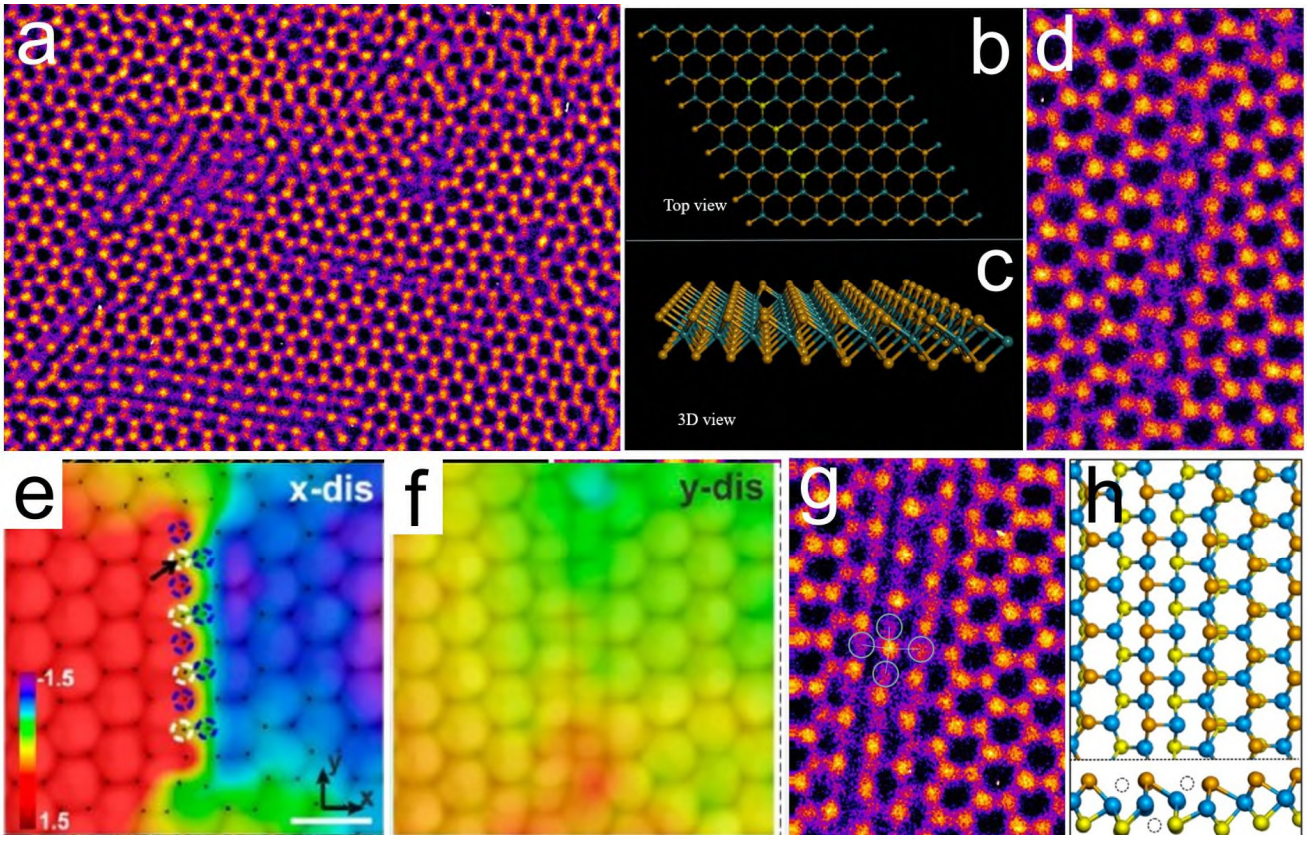

Figure 4. (a) AC-TEM image of line vacancies in monolayer MoS_2 from electron beam irradiation at 80kV. (b) and (c) Atomic models illustrating the 1S line vacancy. (d) AC-TEM image with higher magnification of an isolated 1S line vacancy. (e) and (f) Displacement maps across the 1S line vacancy for x and y directions respectively. Scale bar: 0.5 nm. (g) AC-TEM image of a 3S line vacancy. (h) Atomic

model illustrating the 3S line vacancy with top and bottom staggering of vacancy lines. (a) and (d)-(h) are reproduced with permission from ref. [60] © 2016 American Chemical Society.

While most of the discussion so far has been on S-based vacancies, it is also possible to have Mo metal vacancies in MoS_2, figure 3(m). These are rare compared to S vacancies and are normally accompanied by S vacancies around the metal vacancy. Single Mo atom vacancies have been created on demand using focused electron beam irradiation, figure 5a,b.[59] Control over the local electron sputtering of S destabilizes the Mo bonding and causes it to be displaced to the surface, diffuse away and then open up the metal vacancy site. Prior work has shown that an uneven distribution of W and S vacancies in the CVD-synthesized WS_2 results in the segmentation of PL emission on single crystalline flakes. This has been attributed to the deep trap states and shallow donor states generated by W and S vacancies, respectively.[63] Longer electron beam irradiation causes holes to form in monolayer TMDs, figure 5b, while shorter irradiation can lead to just single metal atom loss, figure 5c,d. Metal atom vacancies beyond single atoms are usually in the form of holes in the lattice. The introduction of large number of S vacancies causes holes to open up in TMDs, with the metal atoms clustering around the edges. This leads to the formation of unique MoS wires that are the last stage of filamentation before the local area ruptures, figure 5e-g.[64,65] Tension in the TMD monolayers can be present from the transfer process to TEM grids and the large hole causes popping and rapid crack formation.[66]

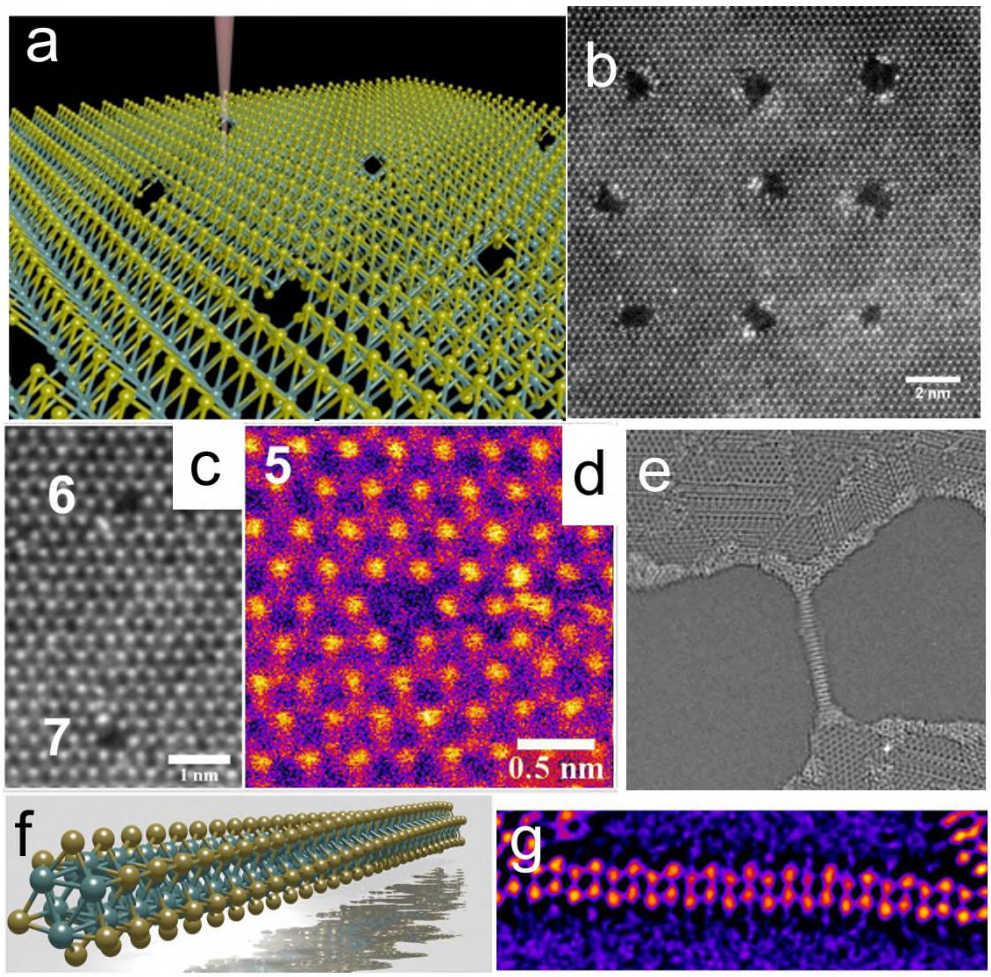

Figure 5. Schematic illustration showing the controlled nanopore drilling in monolayer MoS_2 using the electron probe in STEM. (b) ADF-STEM image after patterning 9 nanopores in a square pattern with 30s drill time for 1 nm holes. (c) ADF-STEM image of two nanopores with 10s drill time. (d) Higher magnification ADF-STEM image of a single nanopore drilled with 10s time, showing displacement of single Mo atom to the surface. (e) AC-TEM image showing MoS wire filamentation during popping of MoS_2 monolayers by excessive vacancy formation by prolonged electron beam irradiation at 80kV. (f) Schematic atomic model of MoS wire with chiral twist. (g) AC-TEM image of the MoS wire suspended across MoS_2 regions. (a)-(d) are reproduced with permission from ref. [59] © 2017 The Royal Society of Chemistry. (f) and (g) are reproduced with permission from ref. [64] © 2016 American Chemical Society.

Recent work showed that cracks propagate along the zigzag direction after rupturing MoS_2 monolayer films that are suspended across micron sized holes, figure 6a,b.[66] The edges of the crack show near perfect zigzag terminations with both S and Mo terminations on either side matching up and indicating that only one row of S atoms are lost during the fracture, figure 6c. In many cases, the crack tip is atomically sharp, figure 6d,e, but it can also have reconstructed tips, figure 6f,g, due to the interaction with dislocation cores at the front during propagation. The crack propagation can be deflected along zigzag directions by vacancies and in areas of large vacancy concentration the crack tips become blunt and the crack speed drops. This work showed that introducing vacancies in MoS_2 that form line vacancies cause cracks to slow down and delay failure and increase fracture toughness.[63] This is quite different to graphene, where large vacancies coalesce down to small number of 5-7 dislocation cores that have minimal effect on crack speed. Dislocations are formed at the front of crack tips, but are rarely formed in other parts of monolayer MoS_2 single crystals. This is because edge dislocation cores require loss of both Mo and S atoms, but in practice it is commonly just S atoms lost in MoS_2. Close to the edges of holes it is possible to observe dislocations, but they are mostly found at grain boundaries.

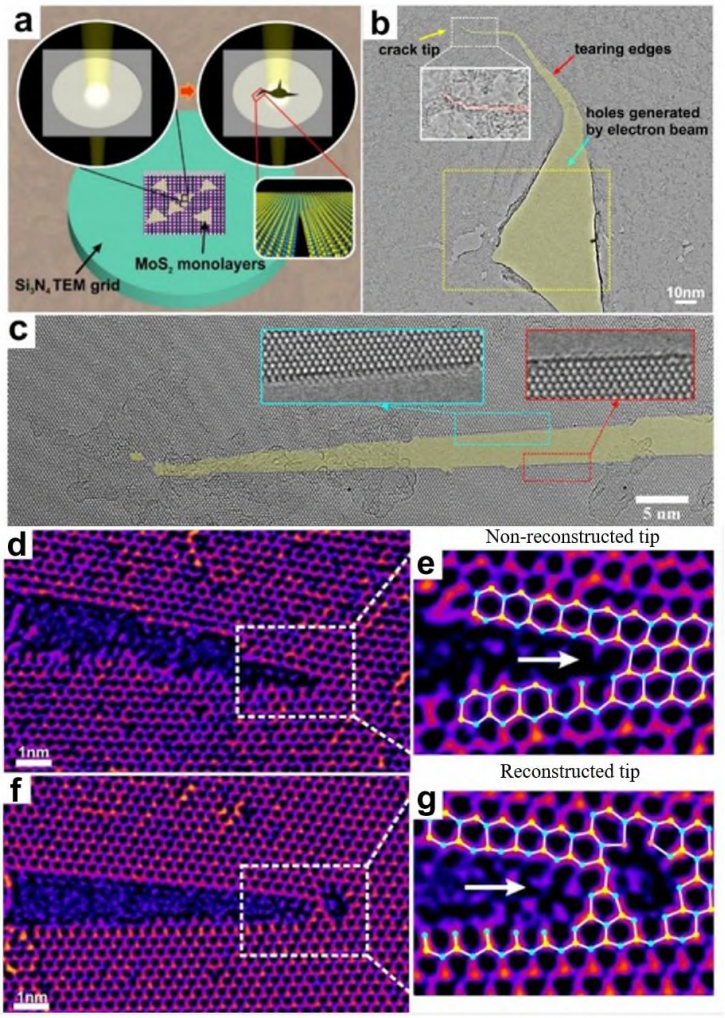

Figure 6. (a) Schematic illustration of the crack formation process on suspended monolayer MoS_2. (b) AC-TEM image of popped area of monolayer MoS_2 by the focussed electron beam and the resulting crack emission. (c) AC-TEM image showing the zigzag lattice propagation direction of the crack tip. (d),(e) AC-TEM image of an atomically sharp crack tip without reconstruction at the tip. (f),(g) AC-TEM image of an atomically sharp crack tip with reconstruction. (a)-(g) are reproduced with permission from ref. [66] © 2017 American Chemical Society.

When two TMD crystals bond together with different lattice directions, some defects must be present to enable this to happen. Mostly, grain boundary stitching is done by the presence of dislocation cores that are spaced apart depending on the relative grain orientations.[67,68] In MoS_2 samples grown by CVD, this is often seen, but there are also findings that show periodic holes are also present in the grain boundary regions. Figure 7a shows a tilted GB of ~7°, with dislocations spaced periodically along the GB interface. Figure 7b, shows a typical dislocation core in a tilted GB region. In special cases where the relative orientation between two grains is 60°, then the antiphase boundary has unique form with S atoms bonded to four Mo atoms, instead of 3, figure 7c,d. This interface is similar to the boundary of an inversion domain. The 60° GB is along the zig-zag direction, but is rarely atomically sharp and instead has steps along the armchair direction that are enabled by 8-member rings, figure 7e. The combination of 4-8 rings permits the GB to adopt any angle at the nanoscale and microscale level, while at the atomic level staying consistent with zig-zag directions (4 member ring) with armchair terraced step-wise movements (8 member ring).[69]

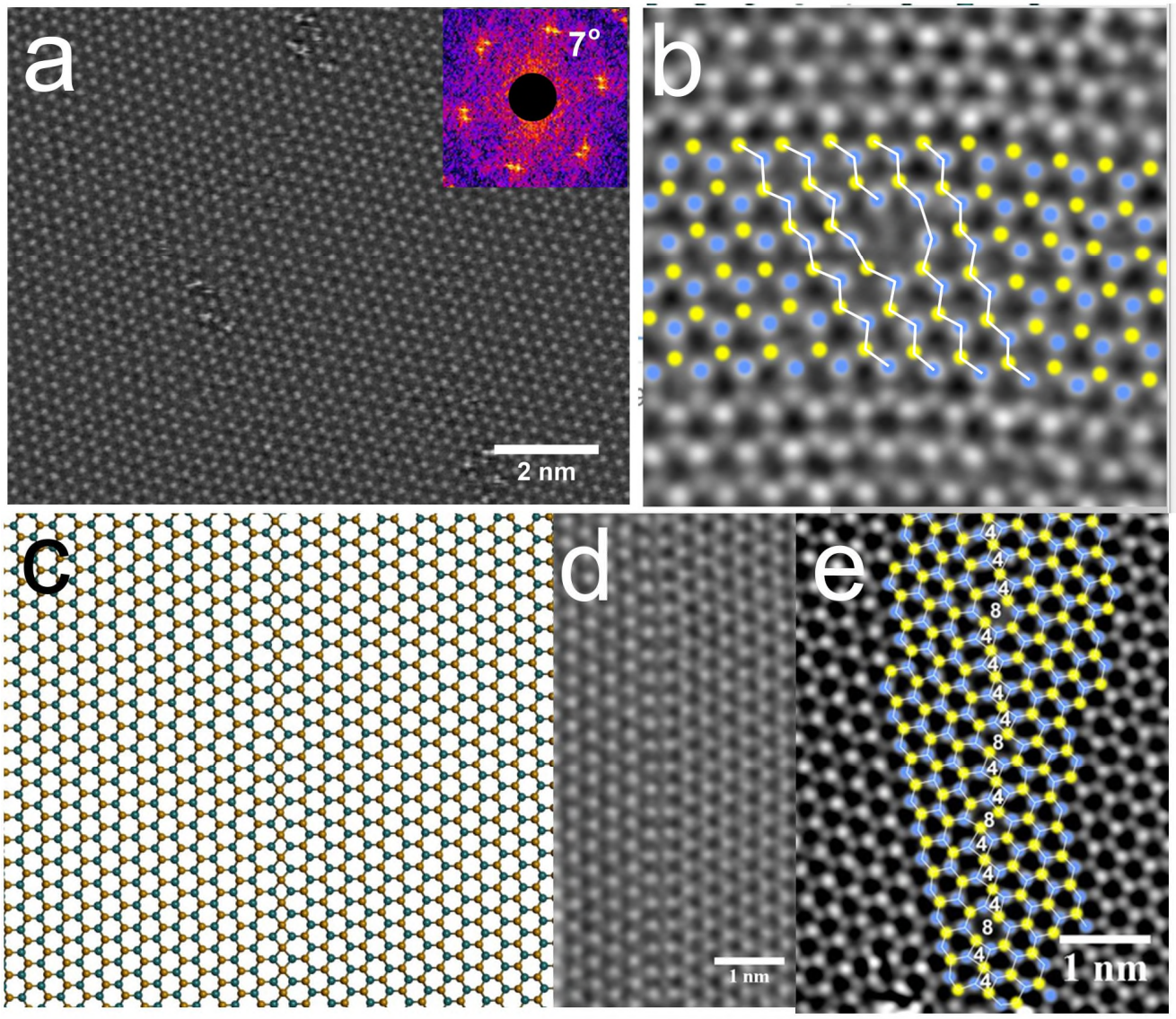

Figure 7. (a) ADF-STEM image of a tilted GB in monolayer MoS_2. Inset shows the FFT with two sets of reflections visible with ~7º rotation. (b) ADF-STEM image of a GB showing a dislocation core, with colour overlay on atoms to indicate S and Mo positions and white lines to show edge dislocation site. (c) Atomic model of a 60º antiphase grain boundary with S atoms bonded to 4 nearest neighbour Mo atoms. (d) ADF-STEM image of the 60º antiphase boundary in monolayer MoS_2. (e) ADF-STEM image with colour overlay of a 60º antiphase boundary with direction deviated from perfect zigzag mediated by 8-member ring.

In bilayer TMDs, vacancies also occur, and give rise to different contrast profiles in TEM compared to monolayer forms. The contrast patterns depend on whether the bilayer is stacked in 2H or 3R form. Recent work showed that S vacancies in bilayer MoS_2 can be found in both the top and bottom layers, indicating that the mechanism of atomic loss by electron beam irradiation is quite complex.[70] Normally knock-on damage is dominant for atoms at the back surface,[57] and atomic loss would be most heavy there, but the observation of S atom loss in the top layer suggests that either vacancies can migrate between TMD layers or that S atomic loss is occurring both on the top and bottom layers, which would suggest it is not simply knock-on sputtering. Single point S vacancies in bilayer MoS_2 can also migrate and aggregate into linear clusters, and the strain from these defect clusters causes some local interlayer stacking distortions. This is seen in AC-TEM as blurring of the local lattice in images.

1.5 EDGES

The presence of two elements in TMDs leads to different edge behaviour compared to graphene, which just contains carbon. Arm chair edges are rarely found, with zigzag edges dominant. The zigzag edges have two possible termination directions, S and Metal, which have different energetics and stability. Recent work using high temperature heating holder for in-situ TEM studies revealed very flat zigzag edges in MoS_2 when heated above 500^{o}C, figure 8a-f.[71] Two distinct contrast patterns are seen at the edge and correspond to the different zigzag terminations. At room temperature, edges from chemical vapour grown samples are typically terminated along the zigzag direction with terraced step edges, as seen in figure 8g. ADF-STEM imaging of the edges at high temperature showed that S depletion causes reconstruction of the S terminated zigzag edges to be double Mo terminated, figure 8h-m. It has been shown that electron beam irradiation can lead to the formation of constrictions in MoS_2 at 800^{o} C, which are highly faceted along the zigzag direction, figure 9a-i. The progressive narrowing results in ribbons that are 1nm in width, defect free and also adopting the Mo rich edge terminations, figure 9j,k. Density functional theory (DFT)

calculations have predicted interesting spin dependent properties for these nanoribbons, with spatially separated spin up and spin down states, figure 9l.

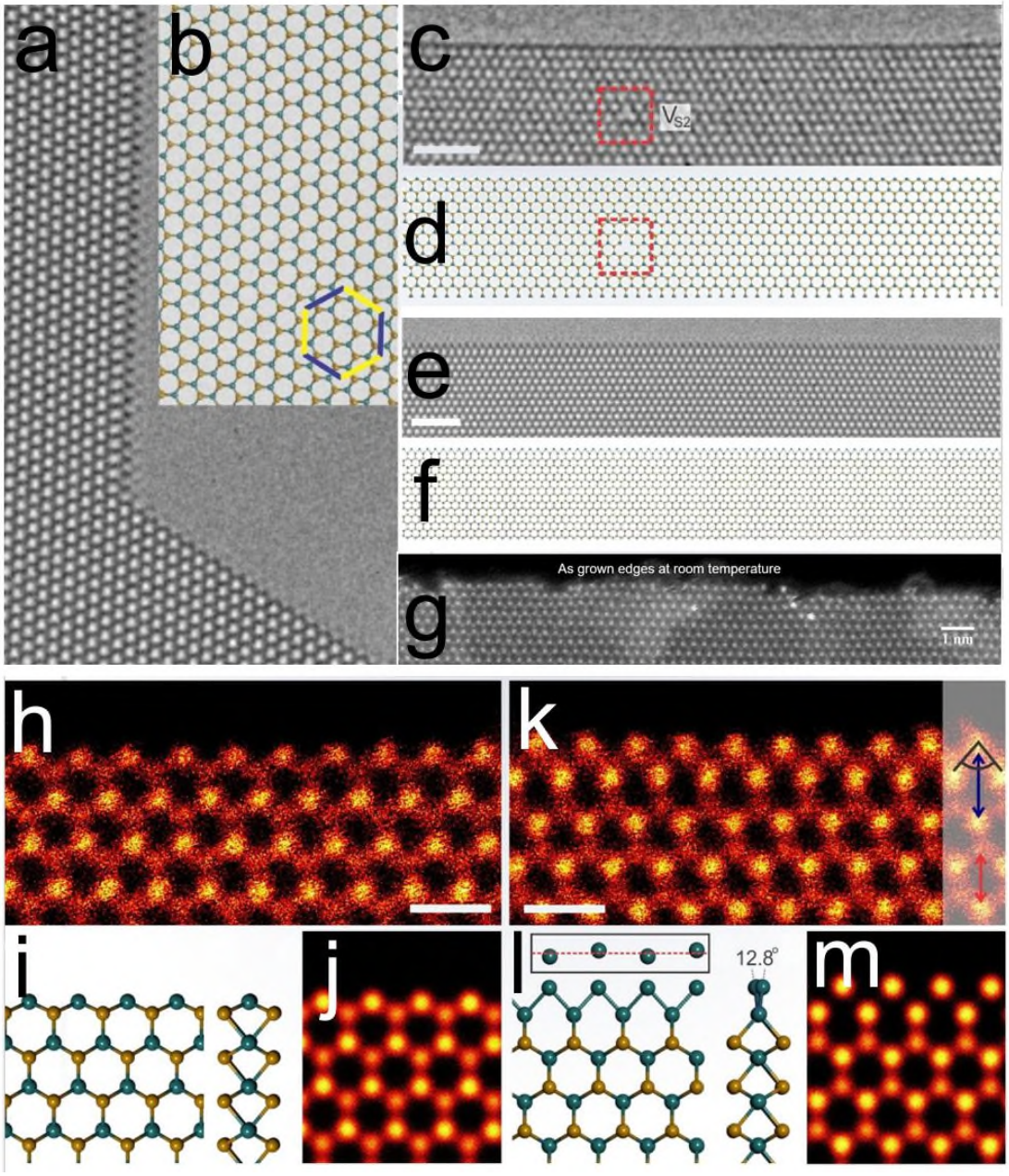

Figure 8. (a) AC-TEM image of MoS_2 edges at 800ºC showing atomically flat terminations with two contrast profiles. (b) Atomic model showing the two different zigzag directions. (c) AC-TEM image of Mo zigzag terminated direction with (d) atomic model. (e) AC-TEM image of S terminated zigzag

direction (actually double Mo) with (f) atomic model. (g) ADF-STEM of as grown MoS_2 edge at room temperature. (h)-(j) ADF-STEM image of Mo terminated edge, with atomic model and image simulation respectively. Scale bar: 0.5 nm. (k)-(m) ADF-STEM image of double Mo terminated edge with atomic model and image simulation respectively. Scale bar: 0.5 nm. (a)-(m) are reproduced with permission from ref. [71] © 2017 American Chemical Society.

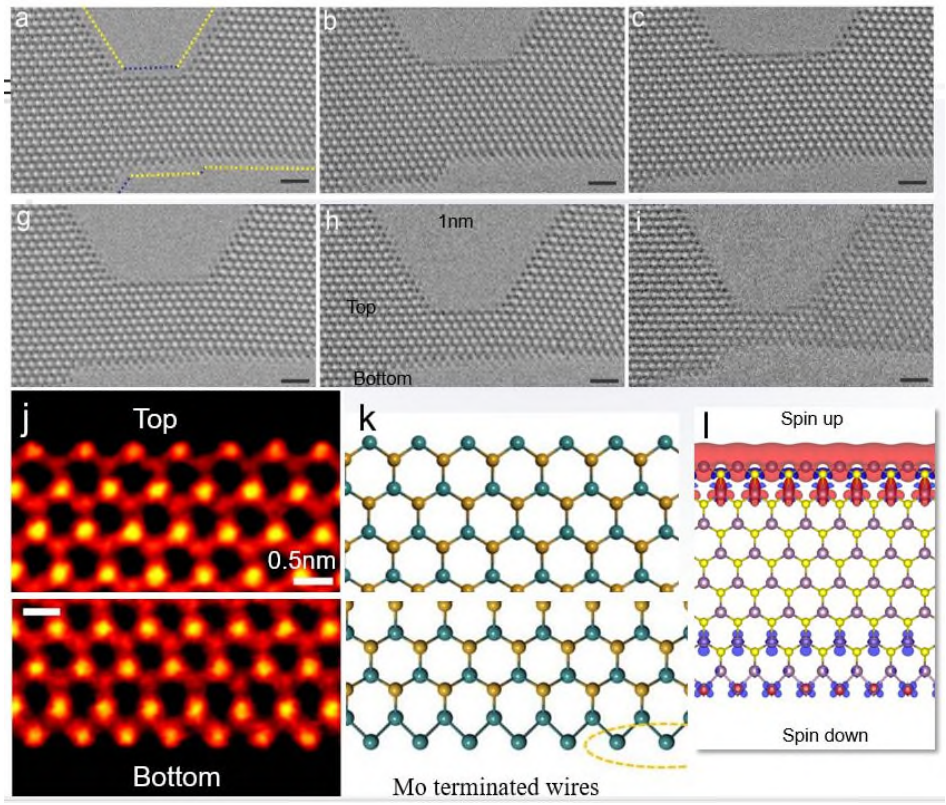

Figure 9. (a)-(i) Time series of AC-TEM images showing the progressive faceted narrowing of a constriction in MoS_2 at 800ºC. Scale bar: 1nm. (j) ADF-STEM images of top and bottom section of a nanoconstriction with (k) showing respective atomic models. (l) DFT predicted spin up and spin down separated states within the nanoconstriction of structure seen in (i). (a)-(l) are reproduced with permission from ref. [71] © 2017 American Chemical Society.

2. Dopants and Alloying in TMDs

This section will cover both substitutional doping in both the S or metal sites in TMDs, interstitial dopants and also surface dopants ranging from single atom dopants to small clusters. The nature of alloying such as MoSeS or MoWSSe materials will be discussed. The use of atomic resolution EELS will be discussed to identify dopant elements and how ADF-STEM can detect variations in dopant concentrations. The high temperature stability of dopants will be discussed. The structure of Pt and Co doped TMDs will be discussed in relation to their catalytic properties and the role of surface carbon on the binding sites. Extrinsic defects can be classified into two categories depending on the location of foreign atoms with respect to the 2D lattice of TMDs. One is defined as 'dopants in lattice', in which foreign atoms serve as substitutional dopants to replace the original transition metal or chalcogen atoms in TMDs. The other one is denoted as 'dopants on the surface', where foreign atoms reside on the surface of perfect 2D TMDs crystals or are trapped on structural defects, such as vacancies, as adatoms due to the locally increased reactivity derived from unsaturated bonds or strain fields at defective sites.

2.1 Dopants in lattice

The successful incorporation of foreign atoms into the TMD lattice normally has two basic requirements. Firstly, the atomic radius of the substitutional atom should be close to that of the atom replaced. Secondly, if the doping concentration needs to be high, the lattice structure of the composite formed by the substitutional element and the unaffected element in TMDs ideally needs to match with that of the pristine TMD, so that the 2D nature of the material can be sustained. Therefore, elements located in the vicinity of the transition metal or chalcogen elements of 2D TMDs in the periodic table are the most promising candidates as substitutional dopants.

Both the transition metal and the chalcogen atoms can be replaced by other elements in the same group of the periodic table with similar radius, valence and coordination manner. $Mo_{1-x}W_xS_2$,[72–76] $MoS_{2(1-x)}Se_{2x}$[77,78] and $WS_{2(1-x)}Se_{2x}$[79] monolayers with x changing from 0 to 1 have been obtained mainly by means of mechanical exfoliation of bulk alloys, atomic layer deposition (ALD), chemical vapor deposition (CVD) and physical vapor deposition (PVD). The electronic structure of TMD alloys can be correspondingly tuned with a continuous but not monotonic shift of the direct bandgap by ~8-10%. Key questions to investigate include: (1) resolving the atomic site of substitutional atoms in the TMD lattice; (2) distinguishing the crystal phase of TMD alloys; and (3) evaluating the distribution manner of dopants in the alloy lattice.

For single layer $Mo_{1-x}W_xS_2$, the trigonal prismatic 1H phase is the most commonly encountered lattice configuration with W and Mo atoms displaying as the brightest and the less bright spots and S_2 as the dimmest or sometimes even invisible sites in the ADF-STEM image due to their decreased atomic numbers (W: 56, Mo: 42, S_2: 32) (Figure 10a,h).[72,73,75] Mo and W atoms share the metal sites, while the double stacked S sites are not perturbed, which has been evidenced by a good consistency between the experimental image and the ADF-STEM image simulation (Figure 10c), constructed based on the corresponding atomic model (Figure 10b). A study reported that monolayer $Mo_{1-x}W_xS_2$ can involve both the semiconducting 1H and the metallic 1T phase simultaneously (Figure 10d).[76] The amount of 1T phase reached the maximum when the atomic ratio between Mo and W approaches 1, and the domain sizes of 1T phase can exceed tens of nanometres (Figure 10d). The structure of 1T phase has been identified by the intensity line profile, as an extra peak corresponding to the single S atom emerges in the centre of the hexagonal ring (inset of Figure 10d). Monolayer $Mo_{1-x}W_xS_2$ alloys with a wide range of specimen contents have a random distribution of Mo and W atoms with no element segregation or separation (Figure 10h-j). This was evaluated by checking the consistency between the Mo atomic ratio obtained microscopically

(by calculating the average ratio of Mo atoms occupied in the nearest round of each W atom in an ADF-STEM image) and the same parameter achieved macroscopically (by x-ray photoemission spectroscopy (XPS), energy dispersive x-ray spectroscopy (EDS) or ADF-STEM analysis across a large area). The closer these two parameter values are, the more homogeneous mixing between Mo and W will be.[73,76] The EDS mapping of the Mo, W and S in a triangular domain also supported the uniform distribution of different elements in the alloy (Figure 10e-g).

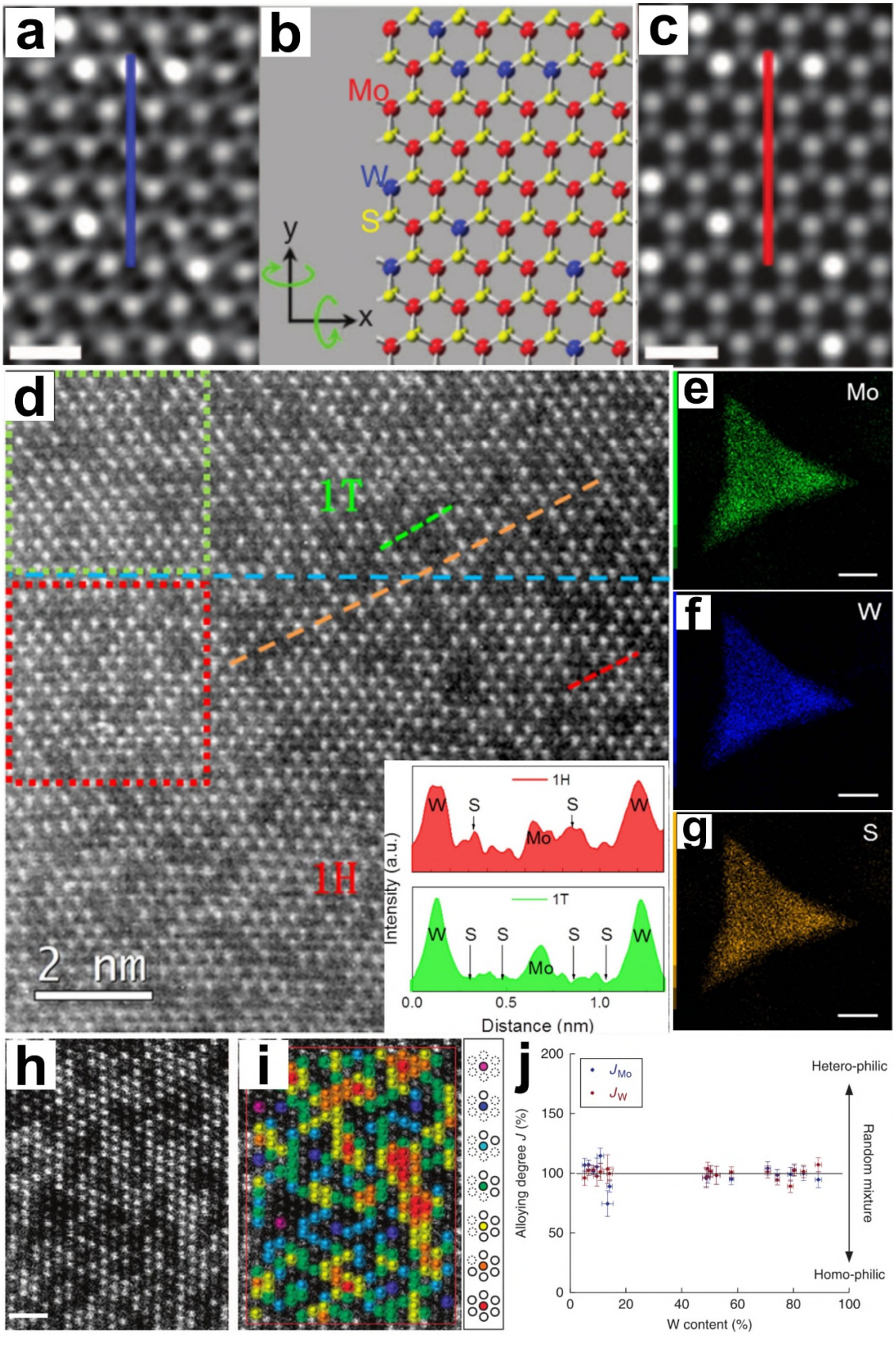
a
b
c
Mo
W
S
y
x
d
1T
1H
2 nm
1H
W
S
S
W
Mo
1T
W
S
S
S
S
W
Mo
Intensity (a.u.)
0.0
0.5
1.0
Distance (nm)
e
Mo
f
W
g
S
h
i
j
Hetero-philic
Random mixture
Homo-philic
Alloying degree J (%)
W content (%)
0
20
40
60
80
100
0
50
100
150
200

Figure 10. (a -c) ADF-STEM image of monolayer $Mo_{0.8}W_{0.2}S_2$, its corresponding atomic model and the simulated ADF-STEM image, respectively. (d) HAADF-STEM image of monolayer $Mo_{0.67}W_{0.33}S_2$ showing the coexistence of 1H and 1T phases with the phase boundary marked by a blue dashed line. Inset exhibits the intensity line profiles taken along the dashed red and green lines in 1H and 1T regions, respectively. (e-g) EDS element mappings of Mo, W and S taken from a triangular alloy flake. (h) ADF-STEM image of monolayer $Mo_{0.5}W_{0.5}S_2$ used for the quantitative analysis of the alloying degree. (i) W atoms marked in purple, blue, light blue, green, yellow, orange and red, indicating six-, five-, four-, three-, two-, one- and zero- coordinate sites. (j) Plot showing the alloying degree of W (J_W) and Mo (J_{Mo}) as a function of the W contents, which is close to 100%, indicating a homogeneous mixture between Mo and W. (a)-(c) and (h)-(j) are reproduced with permission from ref. [73] © 2013 Macmillan Publishers Limited. (d)-(g) are reproduced with permission from ref. [76] © 2016 Macmillan Publishers Limited.

For $MoS_{2(1-x)}Se_{2x}$ monolayers, S and Se atoms share the chalcogen sites, while Mo atom sites are not disturbed.[77,78] Only the 1H phase was observed. Four types of atomic sites with different configurations exist, being Mo, S_2, SSe and Se_2, respectively, which induces the concentrated distribution of the column intensity at four different regions in the intensity histogram (Figure 11a,f). Se_2 sites adopt the highest intensity, while Mo sites are slightly brighter than SSe sites, as confirmed by the quantitative image intensity analysis and the image simulation. S_2 is the dimmest (Figure 11d,e).[78] Chalcogen sites with different numbers of Se substitutional atoms ranging from 0 to 2 have been revealed in a Se dopant mapping with a proper colour rendering of the ADF-STEM image (Figure 11b,c). The distribution of three paired chalcogen sites around Mo atoms with different numbers of Se substitutional atoms matched well with the binominal distribution calculated from the Se content (Figure 11g)., which corresponds to the probability of certain configurations under the assumption of a random arrangement of S and Se atoms. It indicates the homogeneous mixture between S and Se in $MoS_{2(1-x)}Se_{2x}$ monolayers.[77] Bilayer $MoS_{2(1-}$

$_{x)}Se_{2x}$ with a AB stacking sequence has also analysed in a similar approach, and S and Se atoms are still randomly alloyed.[78]

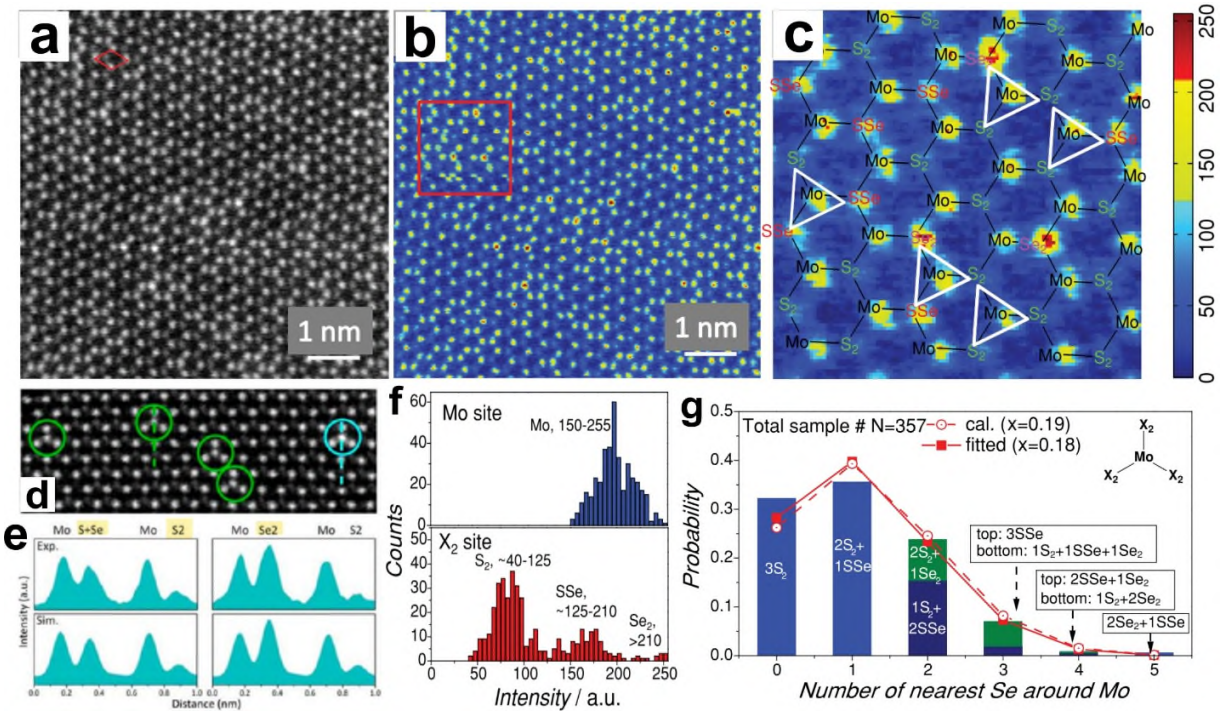

Figure 11. (a) HAADF-STEM image of $MoS_{1.6}Se_{0.4}$ monolayer. (b) HAADF-STEM image in false colour to highlight atomic sites with different structures. Mo sites: yellow; S_2 sites: light blue; SSe sites: yellow, and Se_2 sites: red. (c) Zoomed in image corresponding to the region marked in the red box in (b). (d,e) ADF-STEM image of another Se-doped MoS_2 example with intensity line profiles showing single- (green circles) and double-Se (blue circle) substituted S_2 sites. (f) Intensity histograms of atom sites in (a), representing the percentage of Se dopants in the $MoS_{2(1-x)}Se_x$ alloy. (g) Probability of Mo atoms with different coordination configurations, used for the deduction of the alloy formula for the whole sample based on the local HAADF-STEM image. The red open circles and solid squares correspond to calculated and fitted values using the binomial distribution with an x value of 0.19 and 0.18, respectively. (a)-(c), (f)

and (g) are reproduced with permission from ref. [77] © 2014 John Wiley & Sons, Inc. (d) and (e) are reproduced with permission from ref. [78] © 2014 American Chemical Society.

Molybdenum and tungsten ditelluride alloyed with sulphur or selenium atomic layers ($MX_{2x}Te_{2(1-x)}$, M = Mo, W and X = S, Se) can lead to anisotropic ordering of chalcogen atoms in 1T'-phase material (Figure 12a), while in the 2H-phase, the alloy atom distribution is isotropic (Figure 12b).[80] Chalcogen atoms are divided into two groups based on the unit cell of the metal atoms (Figure 12c). In 1T'-phase, chalcogen atoms in group I has a shorter distance to the neighbouring metal atoms compared to those in group II due to the distorted lattice configuration of 1T', while chalcogen atoms in two groups of 2H-phase material adopt the same distance to the neighbouring metal atoms. Such a structural difference makes S and Se atoms in the 1T'-phase alloy tend to occupy the atomic sites that are closer to the metal atom chain (group I), leaving Te atoms locating in the chalcogen sites in group II, resulting in the anisotropic ordering in monolayer $MX_{2x}Te_{2(1-x)}$ (Figure 12a,d). The anisotropic alloyed behaviour is irrelevant with the Te concentration and is only determined by the phase of the alloy. The reason has been attributed to the shorter bond length formed between S (Se) and Mo (W) compared with that between Te and Mo (W), making S and Se atoms prefer to locate at atomic sites closer to metal atoms so that the total energy of the system can be decreased. The selective occupation of alloyed atoms gives inspirations of growing configuration modulating 2D materials having different types of quasi-1D chalcogen strips interweaving with each other. It also encourages the exploration of tailoring material's physical properties, such as magnetoresistance, by anisotropic alloy structure.[80]

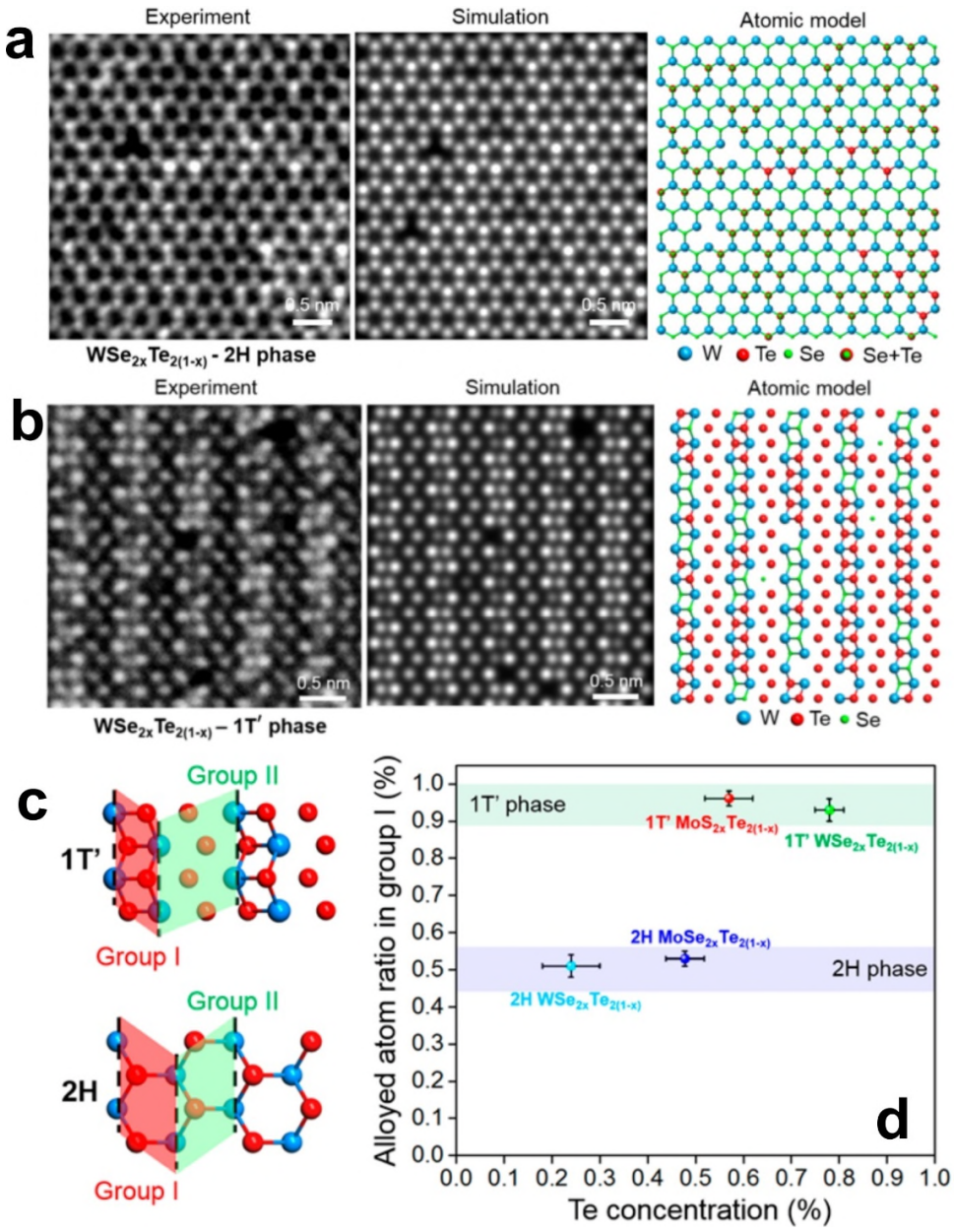

Figure 12. (a) Atomic resolution STEM image, simulation and atomic model of 2H-phase $WSe_{2x}Te_{2(1-x)}$ (Te concentration is ~24%). (b) Atomic resolution STEM image, simulation and atomic model of 1T'-phase $WSe_{2x}Te_{2(1-x)}$ (Te concentration is ~78%). (c) Atomic models showing the division of chalcogen atoms into two groups based on their distances to the metal atom. In 1T' phase, chalcogen atoms in group I locate closer to the neighbouring metal atoms compared to those in group II, while, in 2H phase,

chalcogen atoms in two groups have the same distance to the neighbouring metal atom chain. (d) Statistical plot showing the alloyed atom ratio in group I as a function of the Te concentration, indicating the anisotropic ordering of chalcogen atoms in 1T'-phase molybdenum and tungsten ditelluride alloyed with sulphur or selenium atomic layers. (a)-(d) are reproduced with permission from ref.[80] © 2018 American Chemical Society.

Substitutional dopant atoms have been further expanded to transition metal elements with different electron occupancy of d orbitals than the host transition metal. Manganese (Mn) and rhenium (Re) atoms, both in group 7 of the periodic table with one extra valence electron than that of Mo or W atoms (inset of Figure 13a), have been incorporated into monolayer MoS_2, which could lead to n-type doping of the material. Mn atoms, displaying a 50% intensity compared with Mo in the HAADF-STEM image, not only disperse in the pristine MoS_2 lattice, but also segregate to grain boundaries, performing as substitutional dopant atoms in the place of Mo (Figure 13a,b,d).[81] EDS has been jointly applied to confirm the existence of Mn dopants in MoS_2 (Figure 13c). The doping concentration of Mn is 2 atom%, above which the 2D nature of MoS_2 was unable to be preserved. A recent study showed that Mn-doped MoS_2 significantly relies on the choice of substrates.[81] Inert substrates (e.g. graphene) lead to the successful doping of MoS_2 with Mn, while substrates with reactive surface terminations (e.g. SiO_2 and sapphire) prohibit the incorporation of Mn.[81] For Re-doped MoS_2, most Re atoms serve as stable substitutional dopants at the Mo sites (Re@Mo) without migration under the electron beam illumination for a long period (240s).[82] A minority of Re atoms (～11% among 450 Re dopant atoms) anchor on the surface of MoS_2 lattice as adatoms, which are mobile under the electron beam irradiation and are prone to residing on S sites beside the Re@Mo sites to form a complex of Re-S+Re@Mo (Figure 13e-k). This occurred in the MoS_2 sample with a Re doping concentration of ～0.6 atom%.[82] When the doping concentration decreases to ～0.3 atom%, only isolated single Re dopant atoms were observed without complex or cluster formation.[83] The

incorporation of Re atoms supplies extra electrons to the conduction band of MoS_2 and generates a dopant band slightly below the conduction band minimum (CBM), leading to n-type doping, as revealed by the DFT calculation and the blue shift of the PL peak.[82,83] Moreover, the Re dopants can perform as active sites to attract the absorption of amorphous carbon locally, indicating their potential application in catalysis.

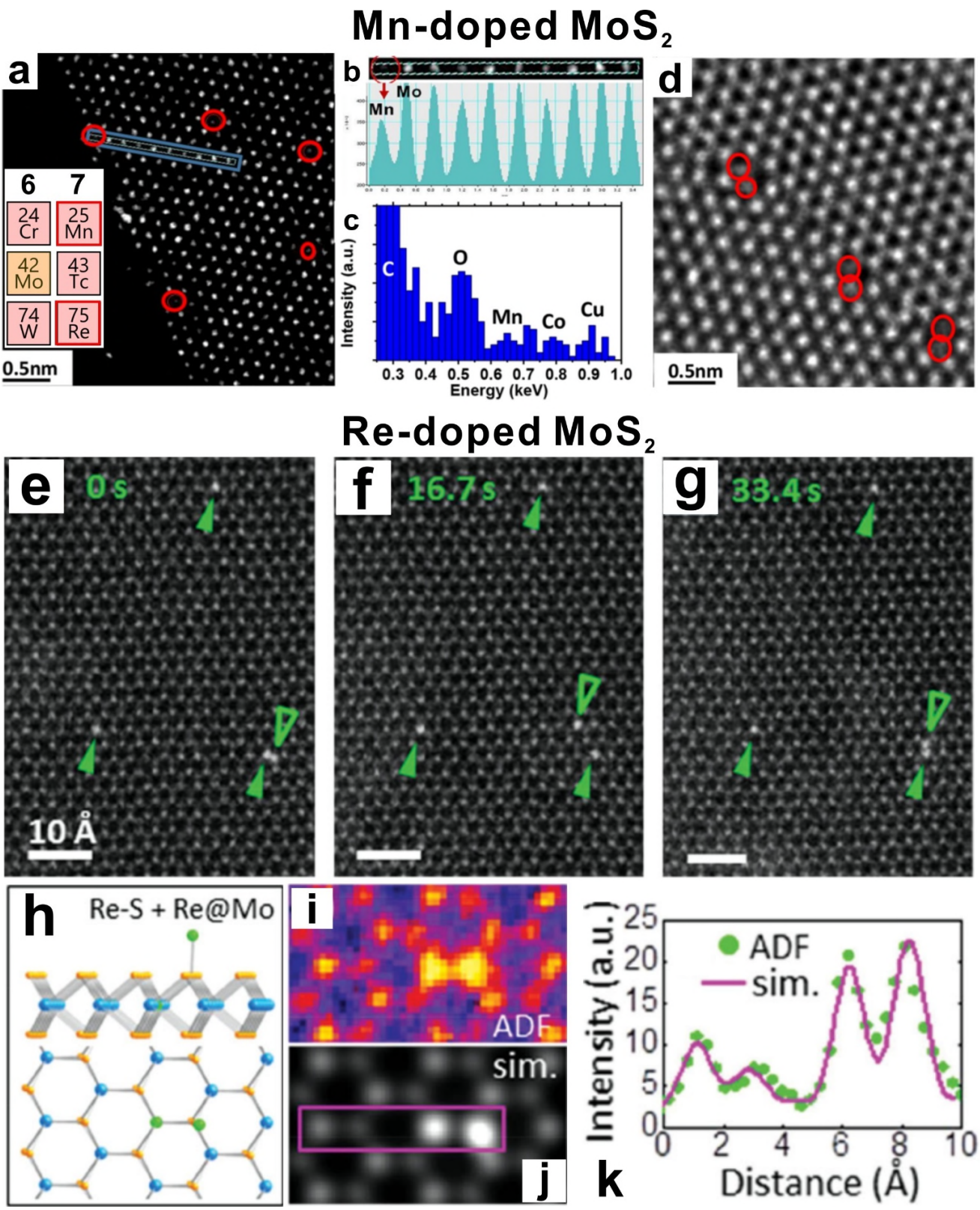
Mn-doped MoS2
a
6
7
24 Cr
25 Mn
42 Mo
43 Tc
74 W
75 Re
0.5nm
b
Mo
Mn
c
Intensity (a.u.)
C
O
Mn
Co
Cu
0.3 0.4 0.5 0.6 0.7 0.8 0.9 1.0
Energy (keV)
d
0.5nm
Re-doped MoS2
e
0 s
10 Å
f
16.7 s
g
33.4 s
h
Re-S + Re@Mo
i
ADF
sim.
j
k
Intensity (a.u.)
25
20
15
10
5
0
ADF
sim.
0 2 4 6 8 10
Distance (Å)

Figure 13. (a) TEM image showing the substitutional Mn dopants (marked by red circles) in monolayer MoS_2 directly grown on suspended graphene TEM grids. (b) Intensity line profiles along the blue boxed region in (c) showing the single Mn atom sitting in the place of Mo with a 50% lower intensity. (c) EDS of the Mn region. The weak Mn signal has been attributed to the detection limit of EDS (≤5%), while the Co and Cu signals come from the grid background. (d) TEM image of showing the Mn dopants (marked by red circles) incorporated at the MoS_2 grain boundary. (e-g) Sequential ADF-STEM images showing the Re substitutional dopants (Re@Mo) in monolayer MoS_2 lattice (solid green arrows) and Re-S adatoms on the MoS_2 surface (open green arrows). (h) Atomic model of Re-S+Re@Mo complex dopant configuration. (i,j) ADF-STEM image and simulated image corresponding to (h). (k) Intensity line profiles corresponding to the experimental and simulated image in (i) and (j), respectively. (a)-(d) are reproduced with permission from ref. [81] © 2015 American Chemical Society. (e)-(k) are reproduced with permission from ref. [82] © 2014 John Wiley & Sons, Inc.

Niobium (Nb), a proposed p-type dopant with five valence electrons (one less than Mo and W), has also been incorporated into monolayer WS_2 supported on sapphire using $NbCl_5$ as the precursor (inset of Figure 14a).[83] Nb serves as substitutional atoms in the W sites (Figure 14a), and can be identified by the Z-contrast variation in ADF-STEM imaging due to the atomic number discrepancy between Nb and W, and other potential dopants, such as Cl, were precluded owning to the intensity mismatch between experimental and simulated ADF-STEM image (Figure 14b). Nb atoms were uniformly distributed in the WS_2 lattice with various atomic arrangements including isolated single Nb atoms, small clusters and 1D chain (Figure 14c-e). It is worth noting that the doping concentration of Nb in WS_2 was 6.7 atom%, which is significant higher than that of Mn and Re in MoS_2 (2 atom% and 0.6 atom%, respectively), and the 2D nature of the Nb-doped WS_2 is well remained.[83] It has been attributed to the good match of crystal structures between WS_2 and NbS_2, both of which share hexagonal layered configuration with similar

lattice constants. In contrast, Mn typically bonds with S in the rock-salt, zinc-blende or wurtzite structures, while ReS_2 has a distorted octahedral structure, all of which are non-layered structures with obvious structural difference with respect to the host TMD material.[77,79] Nb dopants induced the red-shift of the PL peak without degenerating the direct bandgap feature of monolayer WS_2.[83,84]

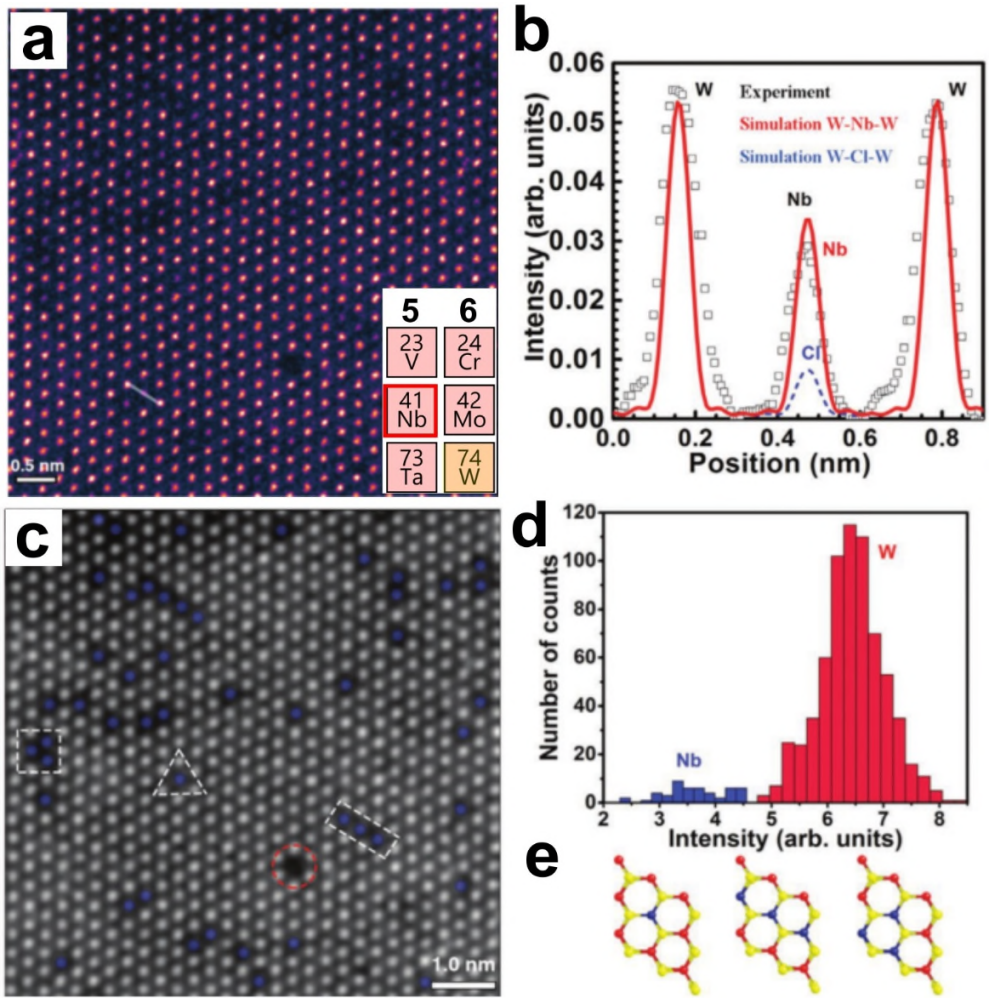

Figure 14. (a) ADF-STEM image of Nb-doped monolayer WS_2. (b) Intensity line profile taken along the white line in (a) (black squares), which fits well with the simulated intensity profile based on Nb-W-Nb configuration (red line). (c) Structural model reconstructed from panel (a) indicating the distribution of

Nb dopants. (blue: Nb sites; white:W sites; black holes: metal vacancies). (d) Intensity histogram of Nb and W atom sites. (e) Schematic illustration of three different configurations of Nb dopants, including isolated points, lines and cluster (blue: Nb sites; red: W sites; yellow: S sites). (a)-(e) are reproduced with permission from ref. [83]

All dopants discussed above were incorporated intentionally in order to tailor the electronic properties of TMDs more widely. However, sometimes unwanted dopants are introduced uncontrollably, which is detrimental to preserving the intrinsic properties of TMDs. Prior work reported that chromium (Cr) and vanadium (V) can form stable single atom substitutional dopants in the place of Mo within CVD-grown monolayer MoS_2 (Figure 15a).[85] Their element types were reliably confirmed by a joint use of ADF-STEM and the atomic-resolution EELS (Figure 15b-f).[85] The use of EELS prevents the misidentification of these defects as being associated with double S interstitials at the Mo sites, which would exhibit very similar contrast in the ADF-STEM image. The Cr and V dopants were stable under electron beam irradiation at 60kV and during in-situ heating up to 800ºC.[85] Cr and V dopants were believed to come from the trace elements in the MoO_3 powder CVD precursor. DFT calculations reveal the potential contribution of Cr substitutional dopants to the n-type doping of MoS_2.[85] Recent work also reported the selective distribution of Cr and Fe impurities in halide-assisted CVD-grown monolayer WS_2, which causes three-fold symmetry segmentation of the PL emission characteristics on hexagonal-shaped domains (inset of Figure 15i). Single Cr substitutional dopants has a larger population in the W-terminated domain (Figure 15g,i), inducing strong trion emission, while Fe atoms, preferring to aggregate into trimer configuration (Figure 15h,i), are more sufficient in the S-terminated domain, which serve as deep acceptor levels and suppress trion emission.[86,87] The Cr and V dopants are also stable when incorporated into S line vacancy defects in monolayer MoS_2, as shown in figure 15j,k..

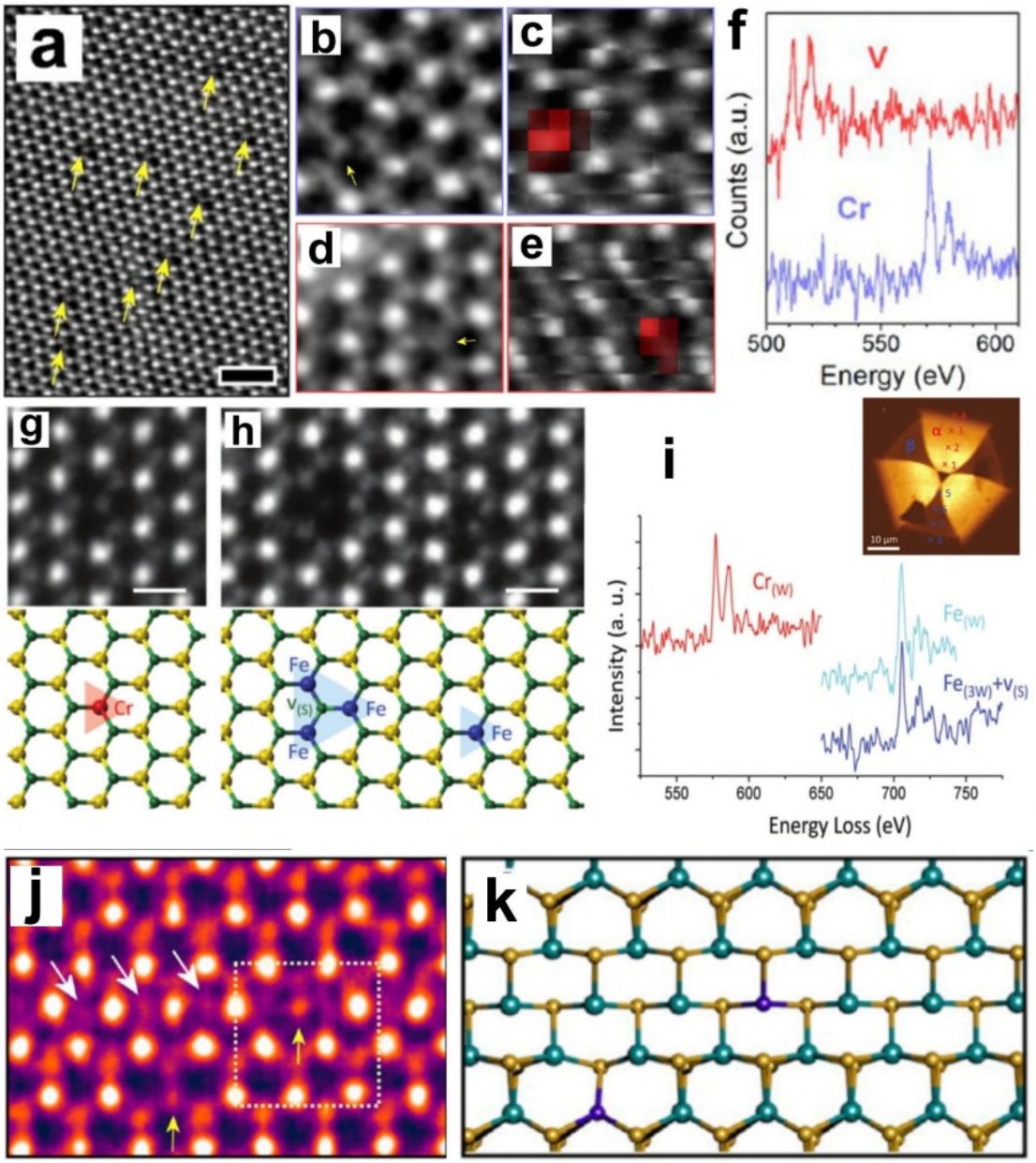

Figure 15. (a) ADF-STEM image of monolayer MoS_2 at 300ºC with single dopant atoms with low contrast sitting at some Mo sites (arrows). Scale bar: 1nm. (b) ADF-STEM image showing the region of EELS mapping. (c) Overlap of the integrated EELS intensity (red) within an energy range of 570 and 590 eV onto the ADF-STEM image captured at the same time, determining the Cr substitutional dopants in the place of Mo. (d) ADF-STEM image showing another region of EELS mapping. (e) Overlay of the

integrated EELS intensity (red) within an energy range of 505 and 525 eV onto the ADF-STEM image acquired at the same time, indicating the V substitutional dopants in the place of Mo. (f) EELS spectra of Cr $L_{3,2}$ and V $L_{3,2}$ edges extracted from the EELS map in (c) and (e), respectively. (g) ADF-STEM image and the atomic model showing single Cr substitutional dopant in the W site ($Cr_{(W)}$) of CVD-grown monolayer WS_2. Scale bar: 0.3 nm. (h) ADF-STEM image and the atomic model showing single Fe substitutional dopant in the W site ($Fe_{(W)}$) and triple Fe substation of three neighbouring W atoms with a S vacancy in the centre ($Fe_{(3W)} + v_{(S)}$). Scale bar: 0.3 nm. (i) EELS spectra of $Cr_{(W)}$, $Fe_{(W)}$ and $Fe_{(3W)} + v_{(S)}$, respectively. Inset shows the segmentation of PL emission intensity (centred at 1.94 eV with a width of 0.15 eV) on monolayer WS_2 due to the selective distribution of Cr and Fe dopants in halide-assisted CVD-synthesized WS_2. (j) ADF-STEM image of Cr dopants inside 2S line vacancy at high temperature of 300^{o}C. (k) Atomic model of the structure in (j). (a)-(f) are reproduced with permission from ref. [85] © 2016 American Chemical Society. (g)-(i) are reproduced with permission from ref. [86] © 2018 John Wiley & Sons, Inc.

2.2 Dopants on the surface

For dopant atoms whose atomic radius or coordination manner do not perfectly match with the host 2D TMD crystal, such as Pt and Au, they tend to sit on the TMD surface rather than being incorporated in lattice, which could lead to lattice strain and out-of-plane distortion. The recent ADF-STEM study reveals that isolated Pt atoms prefer to locate on S vacancy sites on the clean surface of monolayer MoS_2 (Figure 16a-c), which is also energetically favourable, as supported by the DFT calculation.[88] Due to the low migration barriers across the pristine MoS_2 surface, single Pt dopants are highly mobile and can exhibit discrete hopping among different S vacancies nearby dynamically driven by the electron beam irradiation (Figure 16d-j). However, if the MoS_2 surface is contaminated by amorphous carbon, the anchoring position of the single Pt atom loses selectivity, because the configuration is governed by the bonding

between Pt and carbon rather than the interaction between Pt and the MoS_2 lattice. Even though DFT calculations indicate that the catalytic effect for the hydrogen evolution reaction (HER) of S vacancy sites is quenched by the filling of Pt atoms, these S vacancies facilitate the stabilization of single Pt atoms, which are commonly unstable on the intrinsic MoS_2 and tend to agglomerate into clusters.

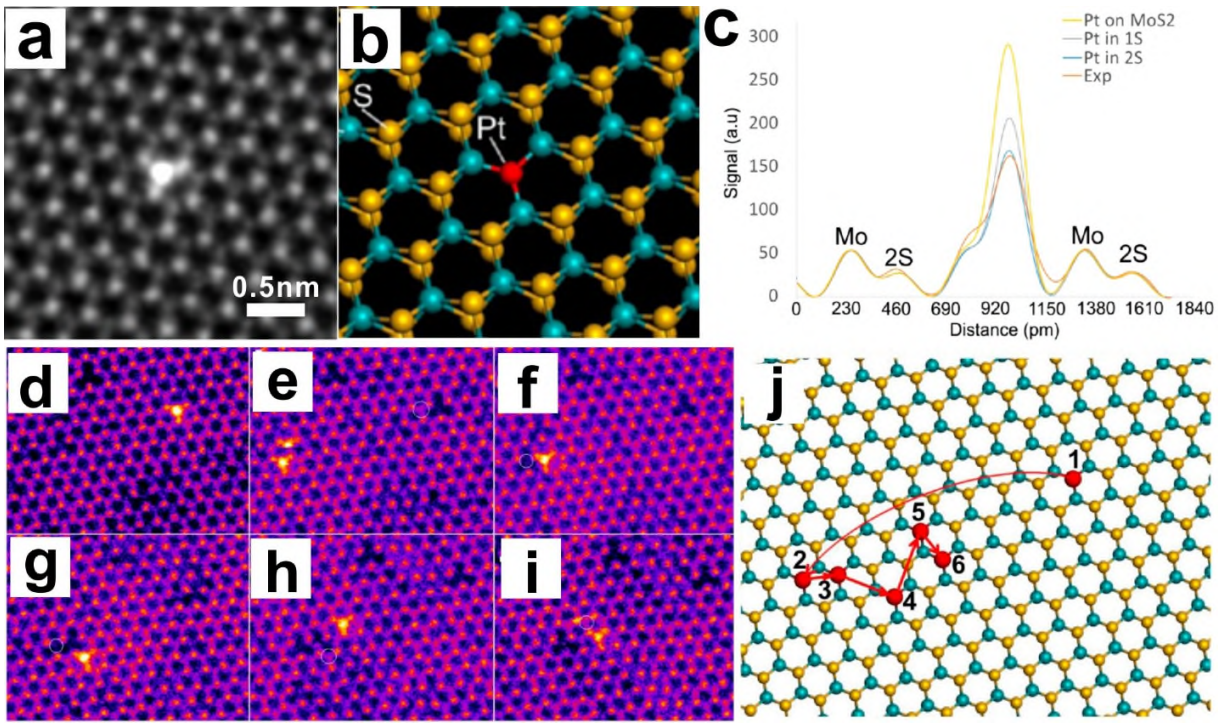

Figure 16. (a) ADF-STEM image of single Pt dopants locating at a S sites with a strong contrast in monolayer MoS_2. (b) Atomic model of (a). (c) Intensity line profile taken from a typical region with a single Pt dopant in MoS_2 in an experimental ADF-STEM image (orange), which is close to the line profile of a simulated image having a Pt substitutional dopant in the double S vacancy (blue). (d-i) Sequential ADF-STEM images showing the dynamics of Pt atom migration on the MoS_2 surface. (j) Schematic illustration showing the Pt movement on MoS_2 based on panel (d) to (i). (a)-(j) are reproduced with permission from ref. [88] © 2017 American Chemical Society.

Single Co dopants in monolayer MoS_2 has also been studied for the design of new hybrid catalyst systems with higher activity and durability for dehydrogenation reactions. Single Co dopants are most favourably trapped at S vacancy sites on the MoS_2 basal plane and edges (Figure 17d,e). ADF-STEM combined with EELS was also able to show other surface sites that Co atom dopants can bind to, including Mo atop sites and the hollow centre of the hexagonal rings (Figure 17a-c,f,g). This recent study has demonstrated that the availability of a large number of unsaturated basal S vacancies in MoS_2 is conducive to accommodating single Co atoms, where they are believed to serve as active centres to increase the catalytic efficiency.[89]

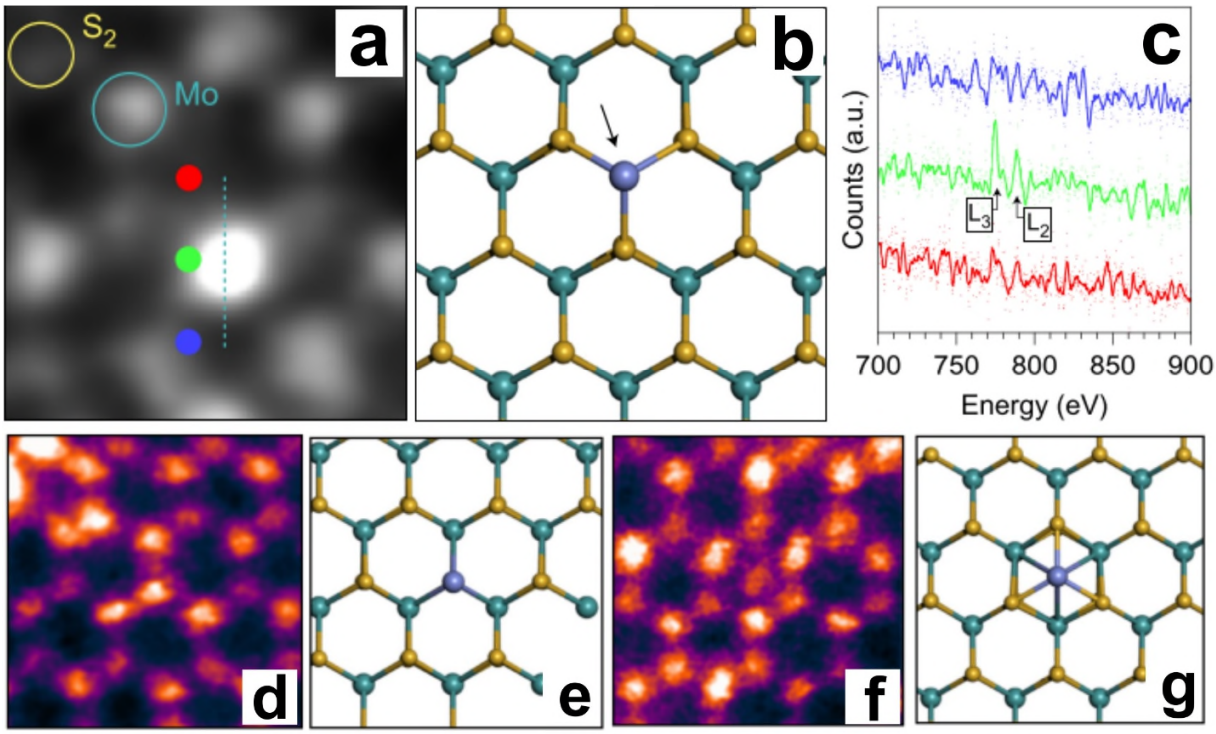

Figure 17. (a) High-magnification ADF-STEM image of a Co atom situated on Mo atop site. (b) DFT-optimized geometry of a single Co atom on Mo atop site. (c) EELS acquired along the line in (a) with EELS signal extracted from above (red), on (green), and below (blue) the Co atom on Mo atop site. Co $L_{3,2}$ edges are indicated, confirming the existence of Co in the scanned column. (d,e) ADF-STEM image

of a Co-substituted S site and its corresponding DFT-optimized atomic model, respectively. (f,g) ADF-STEM image and its corresponding DFT-optimized model of a single Co situated in the hollow site of MoS_2. (a)-(g) are reproduced with permission from ref. [89]

Au atoms are highly unstable on the MoS_2 surface and were found to anchor on either top of Mo, top of S and hollow centre of MoS_2 hexagons due to the similar binding energies at these positions (Figure 18a-d). Only a small proportion of them (～5%) were reported to serve as single substitutional dopants in the place of Mo, as it is energetically unfavourable. Au adatoms are prone to aggregating into clusters rather than dispersing in isolation. They migrated on the MoS_2 surface in a high diffusion rate, making the kinetic pathways not fully distinguishable.[82] The configuration of Au adatoms resembles that of Mo single atoms on intrinsic monolayer MoS_2 (even though Mo adatoms are not extrinsic defects), with Mo sitting on Mo atop sites as the ground state and Mo sitting on S atop sites and on the hollow centre of hexagons as two metastable states. Time-lapsed ADF-STEM images with a time interval of 3s between each frame reveals the migration trajectory of the single Mo atom mainly across the Mo atop sites and the hollow centre of hexagons step by step with no directional preference (Figure 18e-j), which may inspire the investigation of Au adatom dynamics on TMDs.[90]

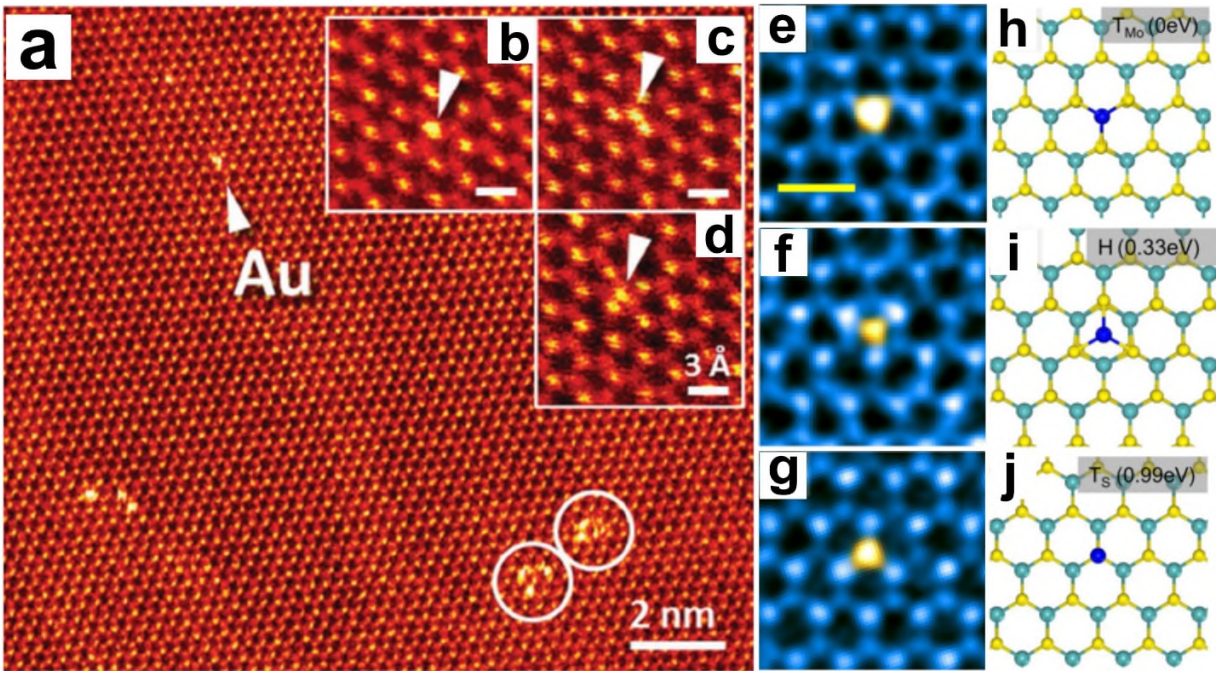

Figure 18. (a) Large-area ADF-STEM image showing Au adatoms (arrow) and clusters (circles) on monolayer MoS_2. Insets show Au adatoms situated on top of the Mo, S and the hollow site of MoS_2 lattice, respectively. (e-g) ADF-STEM images showing the migration trajectory of Mo adatoms from the top of Mo site, to the hollow centre and to the S site. False colour is used to improve the visualization of Mo adatom configuration. Scale bar: 0.5 nm. (h-i) Atomic models corresponding to panel (e) to (g) with relative energies of different adatom states given. (a) is reproduced with permission from ref. [82] © 2014 John Wiley & Sons, Inc. (e)-(j) are reproduced with permission from ref. [90] © 2017 American Chemical Society.

When the amount of adatoms increases, their distribution manner could transform from isolated single atoms to crystalline nanoclusters on the TMD surface, whose configuration and dimensionality are dominated by not only the structural nature of the bulk materials but also the interaction between the nanocluster and the TMD lattice underneath. A recent ADF-STEM study used an in-situ heating holder to track the formation of Pt nanocrystals by the decomposition of the Pt precursor at 800ºC in real time.[91]

Ultrasmall Pt nanoclusters involving ~20 atoms were stabilized into single atomic planes with the help of the monolayer MoS_2 template supported underneath (Figure 19a-c), even though bulk Pt adopts the non-layered face-centred-cubic configuration. 2D Pt nanoclusters were epitaxially grown on MoS_2 with a significant lattice strain in order to better match the crystal parameter of the template MoS_2. When the number of Pt atoms further increases, they aggregated into 3D structure with two types of favourable alignments with respect to MoS_2, and the influence of the MoS_2 template on the lattice constant of Pt nanoparticles eliminated. 3D Pt nanocrystals can etch the surrounding MoS_2 at high temperature or initiated by the electron beam irradiation to form holes, where S atoms are lost to the vacuum and the residual Mo atoms are incorporated into Pt nanoparticles to form alloy (Figure 19d-i). This could lead to increased edge density in single layer MoS_2, which may give rise to improved catalytic activity. Another TEM study reported the formation of monolayer crystalline CuCl nanoclusters, which are ionic crystals with non-layered cubic zinc blende configuration in bulk, by the interaction with the uniform periodic surface of monolayer MoS_2 (Figure 19j,l).[92] They were also epitaxially aligned to MoS_2 with two preferential alignments (Figure 19k) and showed discrete rotation on MoS_2 driven by the electron beam. DFT calculations indicate the coupling between 2D CuCl nanocrystals and monolayer MoS_2 through strong chemical bonding rather than weak van der Waals forces (Figure 19m), which significant impacts the overall property of the material, leading to the type-III band alignment with metallic behaviour for this hybrid system without sensitivity to the stacking pattern. These studies provide insights into the assembly of non-layered-coordinated adatoms to 2D crystalline nanoclusters by making use of the interaction between adatoms and the surface of TMD lattice, which may enrich the library of 2D materials further.

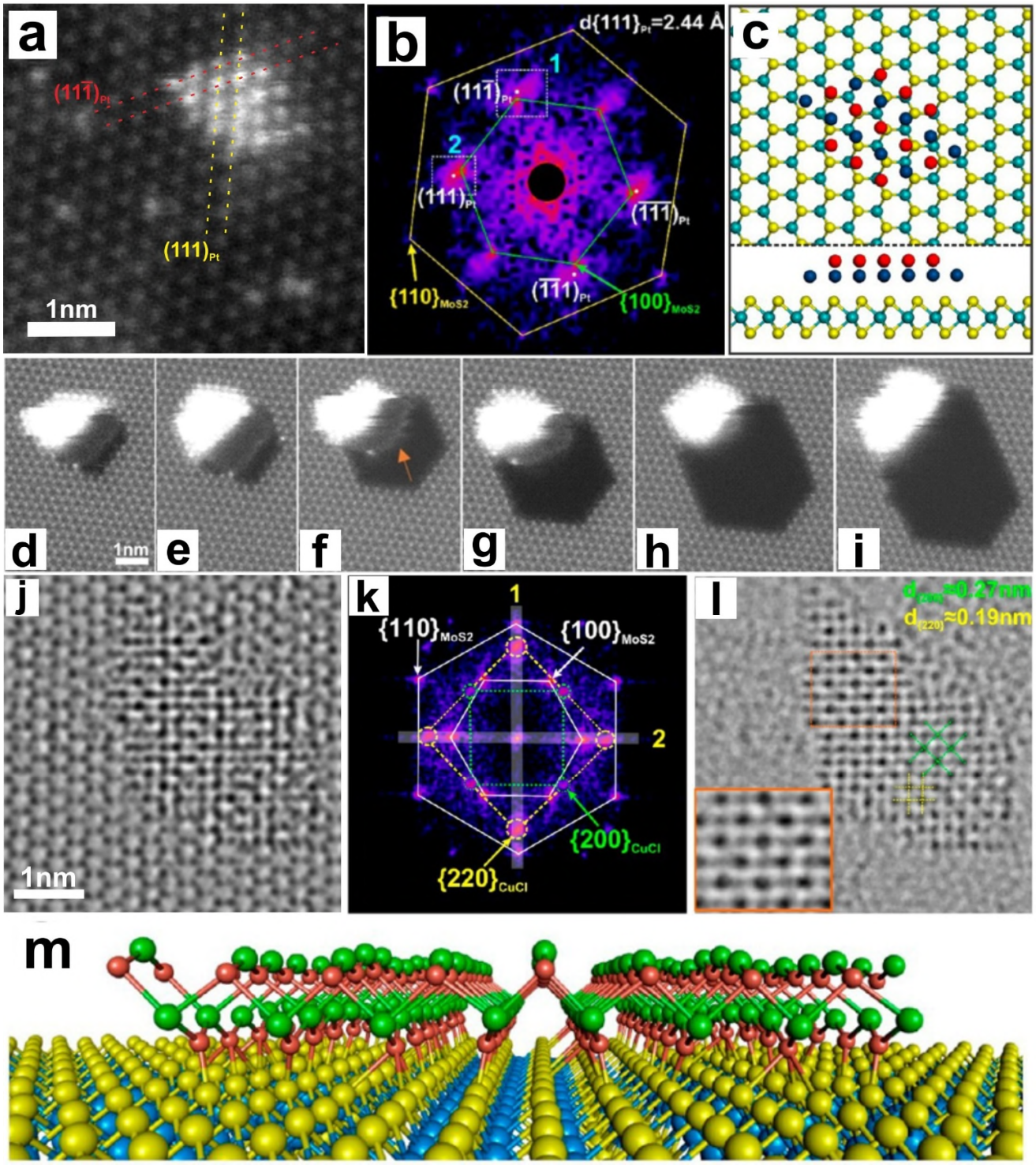

Figure 19. (a) ADF-STEM image of a 2D Pt nanoflake epitaxially grown on monolayer MoS_2. (b) Fast Fourier transform (FFT) of (a). (c) Atomic model showing the two-atom thickness of the non-layered 2D

Pt nanoflake configuration corresponding to (a). (d-i) Sequential ADF-STEM images showing the Pt nanocrystal induced catalytic etching of monolayer MoS_2. (j) Aberration-corrected TEM image of 2D cubic CuCl epitaxially orientated on monolayer MoS_2. (k) FFT of (j) showing one typical preferential alignment between CuCl and MoS_2, which can be defined as $(001)_{CuCl}//(001)_{MoS2}$; $[110]_{CuCl}// [110]_{MoS2.}$ (l) Reconstructed AC-TEM image, which removes the MoS_2 lattice and leaves the 2D cubic CuCl lattice structure only. Inset is the magnified image of the orange boxed region. Green and yellow dashed lines indicate the {200} and {220} family of crystal planes of CuCl, respectively. (m) 3D perspective side view corresponding to the configuration of 2D CuCl on MoS2 in (j). (a)-(i) are reproduced with permission from ref. [91] © 2017 American Chemical Society. (j)-(m) are reproduced with permission from ref. [92] © 2017 American Chemical Society.

3. $MoTe_2$ and WTe_2

Monolayer dichalcogenides typically exhibit either a 1H or 1T stacking structure under standard conditions (Figure 20a). However, Mo and W dichalcogenides formed with the heavier Te chalcogenide will typically form a distorted octahedral geometry,[93] referred to as 1T′ or Td. The regular spacing between the metal and chalcogenide rows seen in 1H and 1T is lost, with alternating metal rows pushed together to form metal rich bands. The chalcogenides within these bands buckle outwards from the plane, as illustrated by comparison of the 1T and 1T' side-on views in Figure 20a. In WTe_2 this pushing together of the metal rows forms pseudo one-dimensional metal chains, which has significant consequences for the electronic properties of the material.[94] With the application of a large magnetic field perpendicular to the plane, and an electric current passed through the metal chains, very high positive magnetic resistances are observed.[95] The relative stability, simplicity, and inherent nanoscale nature of the WTe_2 monolayer suggest promise in applications requiring a robust and orientation sensitive magnetic field sensor. Topological insulating behaviour has been measured in epitaxial monolayers of WTe_2,[96,97] attributed to

the distorted 1T' phase, giving rise to the quantum spin Hall effect – where conductance is quantised as in the quantum Hall effect, but without the need for a magnetic field. It has been proposed to exploit this in a novel transistor based on the quantised conductance.[98] For $MoTe_2$, the preference for exhibiting this 1T' structure seems less pronounced, and so it is possible to tune monolayers of $MoTe_2$ between 1H and 1T' by electrostatic doping.[99] This permits the controllable shifting from semimetallic to semiconducting behaviour, with potential application in memory devices.[100]

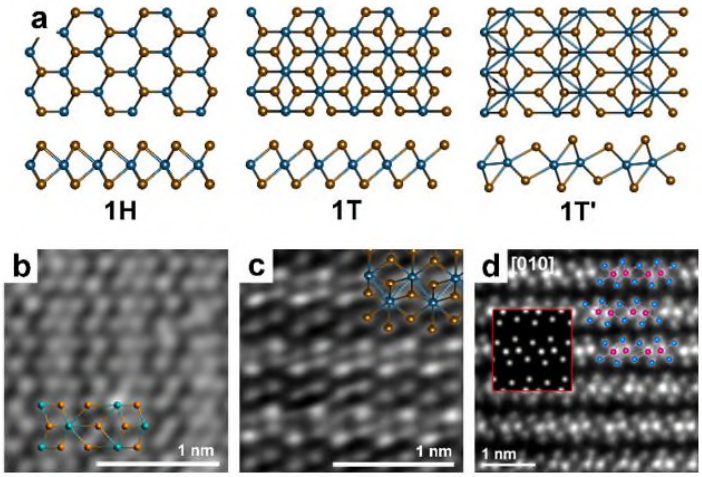

Figure 20. The 1T' atomic structure of $MoTe_2$ and WTe_2. (a) Top and side view atomic models illustrating the differences between the 1H, 1T, and 1T' structures for metal dichalcogenide monolayers. (b) ADF-STEM of monolayer 1T' $MoTe_2$. (c) ADF-STEM of graphene-encapsulated monolayer 1T' WTe_2. (d) ADF-STEM cross-section of a many-layered WTe_2 film, showing the out-of-plane buckling of Te and the spacing of the W rows. (b), (c) and (d) are reproduced with permission from ref. [101] © 2016 American Chemical Society, ref. [102] © 2017 IOP Publishing Ltd, and ref. [103] © 2016 American Chemical Society, respectively.

ADF-STEM imaging has recently been employed to clearly show this distorted 1T' structure. Figure 20b is a view of the basal plane of monolayer $MoTe_2$ prepared by chemical vapour deposition (CVD).[101] As illustrated by the super-imposed atomic model, the ADF image clearly shows the alternating light and dark bands arising from the more densely packed Mo chains. Further work by the same group yielded an even clearer demonstration of the metal chains, this time by employing ADF-STEM imaging of CVD grown monolayers of WTe_2 encapsulated in graphene.[102] The combination of using the heavier W metal, resulting in a greater contrast between the metal chain and the Te due to the greater separation in atomic number (Z = 52, 42, and 74 for Te, Mo, and W, respectively), and sandwiching the fragile monolayer between two sheets of graphene, produces a markedly clearer depiction of the 1T' system. The importance of this graphene encapsulation strategy will be discussed in the following section. To prevent knock-on damage imaging was performed at accelerating voltages of 80 and 60 kV, respectively, although beam damage was still observed to be rapid even at these low beam voltages. While not of an isolated monolayer, the ADF-STEM cross-section image through a bulk WTe_2 sample in Figure 20d well illustrates the out-of-plane bucking of Te seen in the 1T' phase.[103]

4. TMDs beyond Mo and W

Group VIIB transition metal dichalcogenides (i.e., M = Re, Tc) undergo a similar yet subtly different distortion to the 1T structure to the above $MoTe_2$ and WTe_2, forming a diamond-distorted 1T structure (Figure 21a).[104] These Re based dichalcogenides have been shown to exhibit a triclinic layered structure with the Re atoms forming chains, with the Re clustering in diamond patterns.[105,106] As with 1T' compounds, the isolated metal chain manifests interesting phenomena, including anisotropic electronic and optical properties.[107,108] ADF-STEM imaging of mechanically exfoliated monolayers reveals this structure, with the Re clearly forming into diamond clusters in extended metal chains across the basal plane (Figure 21b,c).[109] Grain boundaries were imaged that demonstrated a distinct atomic configuration

to that observed in the 1T or 1H TDMs (Figure 21d), and which were oriented close to 120°, permitting good crystal matching between the grains. Intrinsic changes in direction of the Re chains were observed, in a similar manner to direction change seen across the grain boundary, and as with the grain boundary the rotation was at 120° increments. However a separate study has reported the existence of grain boundaries with inter-grain angles that are not near 120°, with the atomic structure of the grain boundary punctuated by atomic vacancies and larger pores.[110]

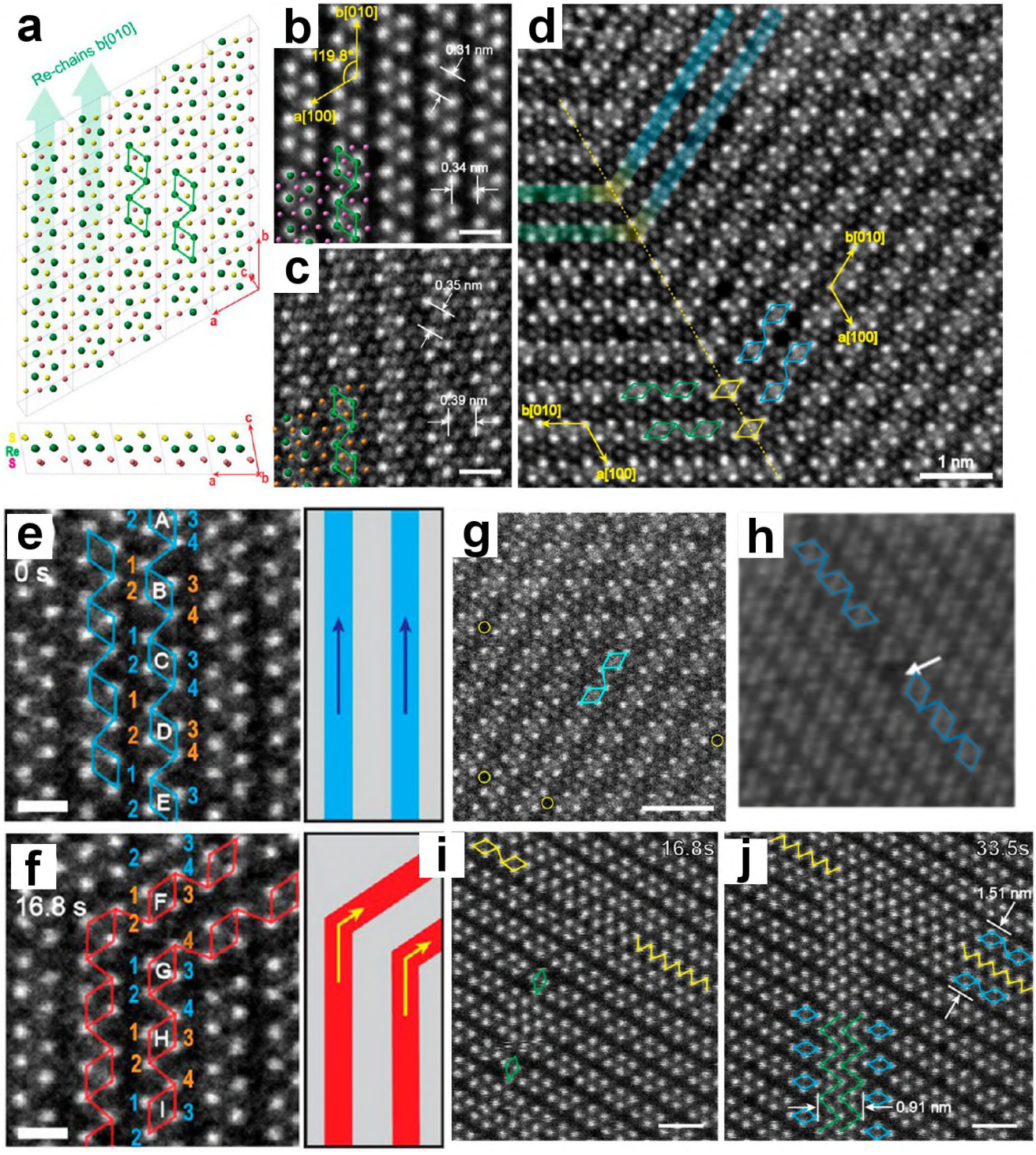

Figure 21. (a-d) The atomic structure of ReS_2 and $ReSe_2$. (a) Atomic models illustrating the basal plane and cross-section views of ReS_2. The Re atoms cluster into diamond configurations along linear chains.

(b,c) ADF-STEM images of monolayer ReS_2 and $ReSe_2$, respectively. Scale bar 0.5 nm. (d) A grain boundary in monolayer ReS_2, indicated by the dotted line. (e-j) Defect formation and behaviour in ReS_2 and $ReSe_2$. (e,f) The before and after HAADF images associated with in-situ heating and electron beam irradiation of ReS_2 at 550 °C, showing an induced rotation in the Re chain by 120°. Scale bar 0.5 nm. (g) Se vacancies in a $ReSe_2$ monolayer (circled). Se vacancies were observed to form primarily in the Se-rich channels. (h) A Re-2S vacancy cluster, located in between a 180° shift in Re-diamond orientation. (i,j) S-deficient phases of ReS_2 formed after extended exposure to electron beam irradiation. Scale bar 1 nm. (a)-(g), (i) and (j) are reproduced with permission from ref. [109] © 2015 American Chemical Society. (h) is reproduced with permission from ref. [110] © 2016 American Chemical Society.

Changes in the orientation of the Re chain could be induced through a combination of in-situ heating and electron beam irradiation. In Figure 21e the Re chains are initially oriented as indicated by the blue annotations, with each Re diamond denoted with a letter and each atom of the cluster labelled with a number. Following heating at 550 °C and electron irradiation for 16.8 s the Re chain was observed to rotate; the Re atom labelled 4 in each diamond cluster move down the image to join the below diamond, and the Re indicated as 3 move up the figure, effectively "rotating" each Re cluster (Figure 21f, red annotations). This may present a way of controllably patterning the anisotropic Re chains for nanodevices.

Imaging of the ReS_2 and $ReSe_2$ monolayers led to significant ejection of S/Se atoms even at low 40 to 60 kV accelerating voltages. Only Se vacancies were observed in the report by Lin *et al*. (Figure 21g),[109] however vacancy clusters consisting of a missing Re along with two neighbouring S atoms were observed by Wu *et al* (Figure 21h).[110] Prolonged exposure to the electron beam was found to induce rotations in the Re diamond clusters. Both these works therefore demonstrate that there is a significant relationship between the grain boundary/Re-line direction and the presence of nearby vacancies. Extended irradiation of ReS_2 was found to lead to the formation of S-deficient phases (Figure 21i,j). S atom ejection

results in the contraction of the Re atom chains into closely packed Re ribbons. If three adjacent Re-diamond chains undergo S depletion then the middle Re chain switches to a 1T'-like triangular phase (Figure 21j, yellow zigzag annotation). S or Se ejection was also observed to occasionally result in one of the Re-diamonds rotating by 90° (Figure 21i, green annotations). The available imaging data suggest that ReS_2 and $ReSe_2$ behave analogously,[109] however combined ADF-STEM and DFT studies of monolayer $ReS_{2(1-x)}Se_{2x}$ alloys suggest that the Se atoms favour occupying sites within the Re-diamond chains.[111]

The group VB transition metal dichalcogenides (i.e., M = V, Nb, Ta) exhibit unique phases that arise following slight distortions in their crystal lattice, including charge density waves[112–115] and superconductivity.[116,117] Due to the fundamental role that dimensional confinement has on the electronic structure in these phases,[118] distinct variations of these properties have been observed in two-dimensional films of these materials;[119] including enhanced superconductivity in monolayers of TaS_2,[120] control over the exhibition of a charge density wave (CDW) phase by a gating field,[121] and significant shifts in phase transition temperatures.[122] The crystal structures and stacking for this family of TMDs are similar to that of MoS_2, showing octahedral (1T) or trigonal prismatic (2H, 3R) symmetries. Characterisation of the atomic defect structures of this family of TMDs may yield insights into the role defects have in the exhibition of these phases,[123] and the variable robustness of the phase-transitions found in these materials as they are thinned to monolayer dimensions.

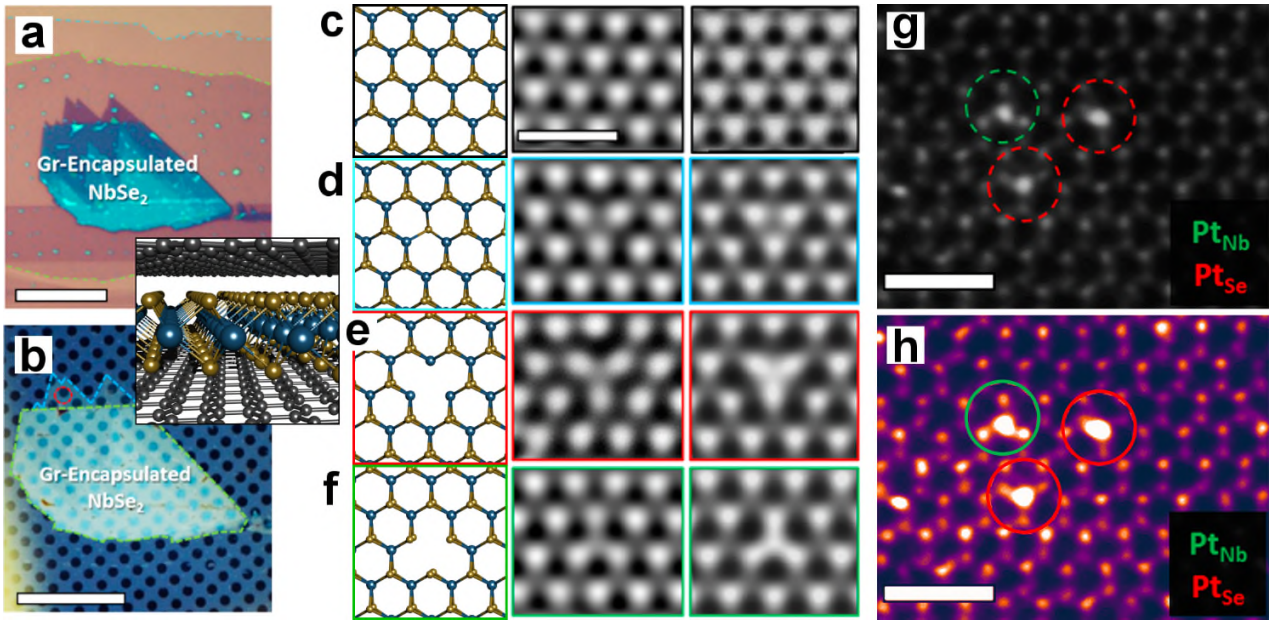

Figure 22. Crystallographic point defects imaged in $NbSe_2$. (a,b) Optical microscopy images of a mechanically exfoliated $NbSe_2$ flake encapsulated between two graphene flakes, laying on a silicon oxide substrate and a TEM grid, respectively. Insert shows a schematic of the encapsulation. Scale bars 20 µm. (c-f) Left to right; atomic model, experimental AC-TEM image, and multislice image simulations, showing (c) a pristine lattice, (d) a Se monovacancy (V_{1Se}), (e) a Se divacancy (V_{2Se}), and (f) a Nb vacancy (V_{Nb}). Atomic models are tilted slightly to show Se lattice occupancy. (g) ADF-STEM image of Pt substitutions (non-saturated contrast). (h) Contrast enhanced version of (g). Scale bars 1 nm. (a)-(h) are reproduced with permission from ref. [124] © 2017 American Chemical Society.

A recent study of atomic resolution defects in $NbSe_2$ with AC-TEM explored the behaviour of the fundamental building block of crystal defects; the atomic vacancy.[124] Key to successfully obtaining data was encapsulating the mechanically exfoliated $NbSe_2$ in graphene monolayers (Figure 22a,b), the significance of which will be discussed below. Representative AC-TEM images, Figure 22c-f, show three categories of single-site defect; the Se monovacancy (V_{1Se}), Se divacancy (V_{2Se}), and the Nb vacancy (V_{Nb}). Vacancy formation was calculated by DFT to be significantly biased toward the preferential

formation and equilibrium of V_{1Se} over V_{2Se} defects; a finding supported by their temporal AC-TEM studies, which revealed the dissociation/healing of Se divacancies into Se monovacancies and the infrequent formation of vacancy line defects. A combination of DFT calculations and geometric phase analysis (GPA) – an analysis technique that maps the crystal lattice strain[125,126] – suggest that Se divacancies that do not dissociate or heal do so due to the stabilising effect of occupying impurity atoms such as O or C, the presence of which are inferred due to the magnitude of the lattice strain around the divacancy. ADF-STEM was also employed to reveal the preferred occupancy for Pt atomic substitutions, with the images revealing that Pt can reside in either the Nb or Se site (Figure 22g,h). Pt atoms occupying basal plane adatom positions, such as in a top or hollow site, were not observed, which may be a result of the energetic favourability of substitution.

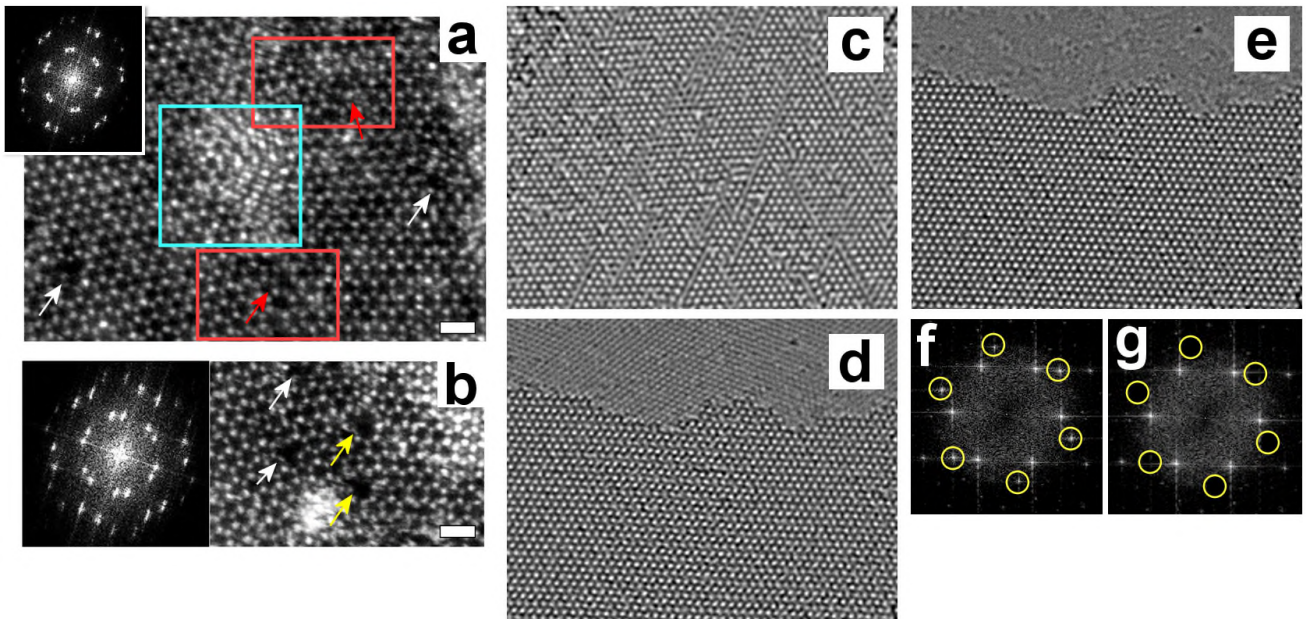

Figure 23. (a-b) ADF-STEM images of grain boundaries in a graphene encapsulated $NbSe_2$ monolayer. (a) A grain boundary, demonstrating both atomic stitching (red rectangles) and overlap (cyan rectangle) configurations between the two grains. White arrows indicate vacancy defects, red arrows indicate bridging atom defects formed to accommodate the strain in the grain boundary. The insert is a Fourier

transform of the image, showing the two rotationally misaligned crystals. (b) An atomically stitched grain boundary and accompanying Fourier transform. White arrows indicate vacancies. Yellow arrows indicate 5-8 defects, similar to the 5-7 dislocation cores that are typically found in grain boundaries of hexagonal crystal systems. Scale bars are 0.5 nm. (c-g) Effect of graphene encapsulation on defect formation. (c) AC-TEM image of monolayer MoS_2 after electron beam irradiation of total dose 2×10^8 *e* nm^{-2}. Many vacancy defects are apparent. (d) AC-TEM image of monolayer MoS_2 encapsulated in graphene, subjected to the same dose as (c), showing very few defects. The graphene lattice can be seen at the top of the image beyond the MoS_2 edge. (e) Fourier filtered version of (d), removing the graphene lattice contribution to the image. (f) FFT of (d), showing reflections corresponding to the MoS_2 and the graphene, the latter indicated with circles. (g) FFT of (e), with the graphene reflections indicated removed by Fourier filtering. (a) and (b) are reproduced with permission from ref. [127] (c)-(g) are reproduced with permission from ref. [128]

The grain boundaries of $NbSe_2$ prepared by CVD have been also recently been studied by ADF-STEM,[127] again via graphene encapsulation to militate against beam damage and prevent oxidation. As well as the vacancies and interstitial defects imaged in ref. 124, this work was able to capture the atomic structure of a $NbSe_2$ grain boundary (Figure 23a,b). In Figure 23a, the grain boundary runs vertically through the centre of the image, with the left grain rotated from the horizontal compared to the right. This rotational misalignment is illustrated in the Fourier transform insert, which depicts the two rotated sets of hexagonal reflections. Two configurations of grain boundary were observed, indicated with red and cyan boxes. The red boxes show atomically stitched grain boundaries, where the atomic edge of one grain forms bonds with the other. By contrast, in the cyan area the adjacent grains instead overlap, producing an interference pattern that can be disentangled and interpreted by Fourier filtering of the image. These two types of grain boundary are similar to those observed in TEM studies of graphene.[129] The atomic stitching

between the two grains exhibits two different bonding arrangements. For Figure 23a the bonding arrangement employs bridging atoms (red arrows), where an under-coordinated atom spans a larger vacancy structure,[130] in extended vacancy chains. In Figure 23b we see defects that are similar to the expected 5-7 dislocation cores that have been modelled and observed in graphene, silicon, and other hexagonally symmetric crystal structures.[131–133] However, detailed inspection of these cores suggests that they are in fact distorted 5-8 defects – there are eight bonds in the larger ring rather than seven. This structure does not appear to have been anticipated in the theoretical literature for TMD grain boundaries.[134] As the 5-8 cores do not appear to have any bond reconstruction across the 5-membered ring, and the bridging atom configuration has been shown to maximise bond coordination in more amorphous structures,[130] we suggest they are evidence of the difficulty in achieving full atomic stitching during the CVD growth of $NbSe_2$, which is further supported by the observation of grain overlap instead of atomic stitching in Figure 23a.

Many two-dimensional layered materials that have been isolated experimentally have yet to be characterised at the atomic level. In some cases, this is due to the difficulty in obtaining atomic resolution images before the sample is destroyed by the electron beam. Beam damage in the TEM occurs through several mechanisms, including elastic collision "knock-on" damage, heating, charging, and radiolysis, and disentangling which is the dominant mechanism in a particular sample can be challenging.[135]

For the prototype two-dimensional material graphene beam damage is almost exclusively due to knock-on collisions; energy is transferred from an incident electron to an atom in the sample during a collision by conservation of momentum.[136–141] If this energy transfer is sufficient the collision will eject the atom from the sample. The prevalence of this type of damage is mainly dependent on the energy of the electron beam, the sputtering cross-section of the sample's atoms, and the sample's atomic structure. The atomic thickness and low atomic number of the constituent carbon atoms of graphene, which have higher

sputtering cross-sections, make it susceptible to knock-on damage. However by sufficiently decreasing the electron energy knock-on can be negated entirely, as the electrons will never impart sufficient energy to overcome the threshold required to eject an atom. The strong sp^2 bonding arrangement ensures that this energy threshold for graphene is relatively high,[142] and as a result atomic resolution TEM imaging of graphene can be carried out extensively provided that the beam energy is sufficiently low, below 80 keV,[136] at which energy a modern TEM is still able to resolve atomic features. This is a significant reason for why the large majority of atomic resolution defect studies in two-dimensional materials have been of graphene.

That the beam damage in graphene is so overwhelmingly dominated by a single mechanism, knock-on damage, is unusual. The intrinsic properties of graphene negate other damage mechanisms; its exceptional electrical and thermal conductivities efficiently dissipate excess charge and heat, and its inert sp^2 bonding structure ensures relative resilience to reactive radicals produced from the radiolysis of surface contamination and trace gases. And that the knock-on damage mechanism can be completely negated through imaging at a moderate beam energy is also unusual for many low-dimensional materials; most lack the strong chemical bonds of graphene, yet still possess low atomic number elements with high sputtering cross-sections, leaving them vulnerable to knock-on ejection even at low electron energies of 80 keV.

It was initially shown by two groups that encapsulating these more vulnerable two-dimensional materials in a monolayer graphene sandwich structure led to greatly reduced electron beam damage.[46,128] Figure 23c shows a typical AC-TEM image of MoS_2 after imaging, with many defects. The graphene encapsulated MoS_2 by contrast shows virtually no defects after being subjected to the same total dose (Figure 23d). The graphene monolayer acts much the same as a gold-coating applied to a sample studied in a scanning electron microscope, in that it helps to dissipate any excess charge build-up that might lead to dielectric

breakdown, as well as acting as a heat-sink. Graphene can also act as a shield, screening the fragile contained membrane from oxidation outside the microscope vacuum,[124] and radicals generated by radiolysis of surface residues. Finally, the low atomic (*Z*) number of carbon make it effectively invisible in *Z*-contrast HAADF-STEM imaging of most samples (Figure 22g), and its regular crystal structure means that the contribution of its lattice can easily be subtracted from a TEM image by Fourier filtering (Figure 23e-g). The use of graphene encapsulation for atomic resolution studies of materials beyond MoS_2 is still in its infancy, however its use to reveal the atomic structure of $NbSe_2$ and WTe_2,[102,124] as covered earlier, demonstrates the validity and potential of this approach.

5. Other 2D Metal Chalcogenides

Few atomic resolution studies have been performed on two-dimensional metal chalcogenides beyond the above. Layered non-transition metal chalcogenides (i.e., M = Ga, Bi, Sb, In, Ti) are beginning to be more widely isolated into few- and mono-layer phases,[143–148] however these have largely yet to result in atomic level defect studies, partly due to the difficulty of preparing uniform monolayers, cleanly transferring them, and keeping them intact while suspended on the TEM grid.[149] There is potential for rigorous TEM investigations to be performed, as the crystal structures can often exist in a variety of phases and stacking orders, as with the TMDs, and potentially novel defect geometries, which may have implications on the material properties. For instance, Ga vacancies have been suggested to inhibit the performance of few-layer GaTe electronic and optoelectronic devices,[150] and the relationship between vacancies, antisite defects, and doping are thought to be pivotal for exhibiting conducting surface states in the topological insulator Bi_2Se_3.[151,152]

Monolayer α-In_2Se_3 can be grown by physical vapour deposition, with only the alpha phase having been so far isolated as a monolayer,[153,154] and has been studied by ADF-STEM imaging (Figure 24).[155] The ADF-STEM images (Figure 24a) reveal the hexagonal symmetry of its structure, and the atomic number

Z contrast helps to clarify the atomic column structure (Figure 24b). The cross-sectional view of the structure reveals that it has a 'quintuple layer' arrangement of atoms, with two distinct atomic columns. The fainter column in ADF-STEM contains just a Se and In atom, and the brighter is a Se-In-Se column. Interestingly, occasional brighter atomic columns were observed (Figure 24c), suggesting either substitutional doping with a heavier element, or an adatom situated on the Se-In-Se column (a top site adatom). The authors found extensive large clusters of In, ranging from 10 nm to 1 μm, as confirmed by EDS, and so speculate that the brightness is caused by an additional In atom bonding to the top atomic layer of Se (Figure 24c insert).

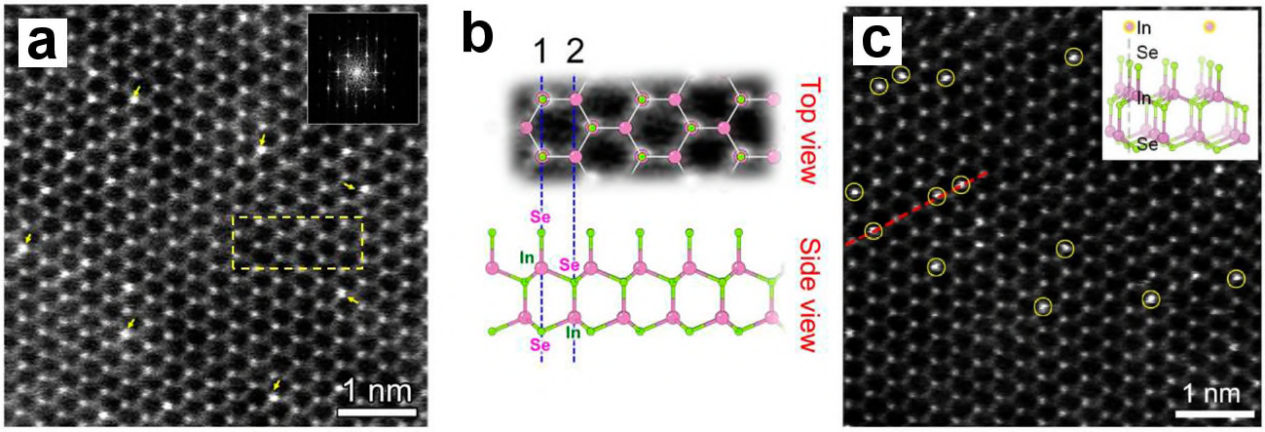

Figure 24. (a) ADF-STEM of monolayer In_2Se_3 and Fourier transform (insert). Yellow arrows indicate surface adatoms. (b) Magnified view from the boxed region of (a), annotated with atomic positions. A cross-section view atomic model of the section is shown beneath the image, illustrating that the brighter atomic columns are Se-In-Se. (c) High intensity, atomic columns indicated with circles, all exclusively occupying the Se-In-Se lattice site. It has been suggested that these are surface dopant adatoms, likely In. (a)-(c) are reproduced with permission from ref. [155] © 2015 American Chemical Society.

Many layered compounds that might be suitable for monolayer isolation have unusual crystal structures, and so it can be difficult to intuitively reason whether they will readily form stable isolated

monolayers. Naively assuming that the monolayer structure will be structurally equivalent to the bulk or few-layer structure was demonstrated to not necessarily be true in all cases by Lin *et al.*[156] They mechanically exfoliated $PdSe_2$, a compound that has been predicted to be stable in monolayers and exhibit semiconducting properties,[157–159] and performed atomic resolution ADF-STEM imaging to confirm the atomic structure. The expected monolayer structure for $PdSe_2$, shown in Figure 25a, forms a square backbone network. ADF-STEM imaging (Figure 25b) revealed that this structure was found in few- to bi-layer regions of the exfoliated sample, however a distinct atomic configuration was observed for the monolayer region. The layer-by-layer thinning is confirmed by the concomitant reduction in contrast (intensity) with each layer lost (Figure 25b). However, interestingly the intensity reduction step from bilayer to monolayer is 1.5 times smaller than the intensity decrease seen from e.g. trilayer to bilayer. As the intensity in ADF-STEM is linearly proportional to thickness of a few-layer, this suggests that the monolayer possesses a different atomic structure and elemental constituents, in order to make up for this expected contrast difference. The atomic pattern observed is also clearly distinct than that expected from the $PdSe_2$ structure shown in Figure 25a. DFT calculations combined with STEM image simulations allowed the authors to confirm that the monolayer is in fact a distinct atomic structure; a Se deficient Pd_2Se_3 composition (Figure 25c). Figure 25d shows the expected ADF-STEM image for a $PdSe_2$ monolayer, which does not agree with the observed images. DFT calculations suggested that this structure formed from the fusion of the two layers in a bilayer, with ejection of the excess Se atoms, and was confirmed via in-situ ADF-STEM imaging. Observing Pd_2Se_3 forming from bilayer $PdSe_2$ was confirmed by subjecting regions to electron beam irradiation, leading to preferential ejection of Se atoms and artificially enabling the creation of Se deficient areas.

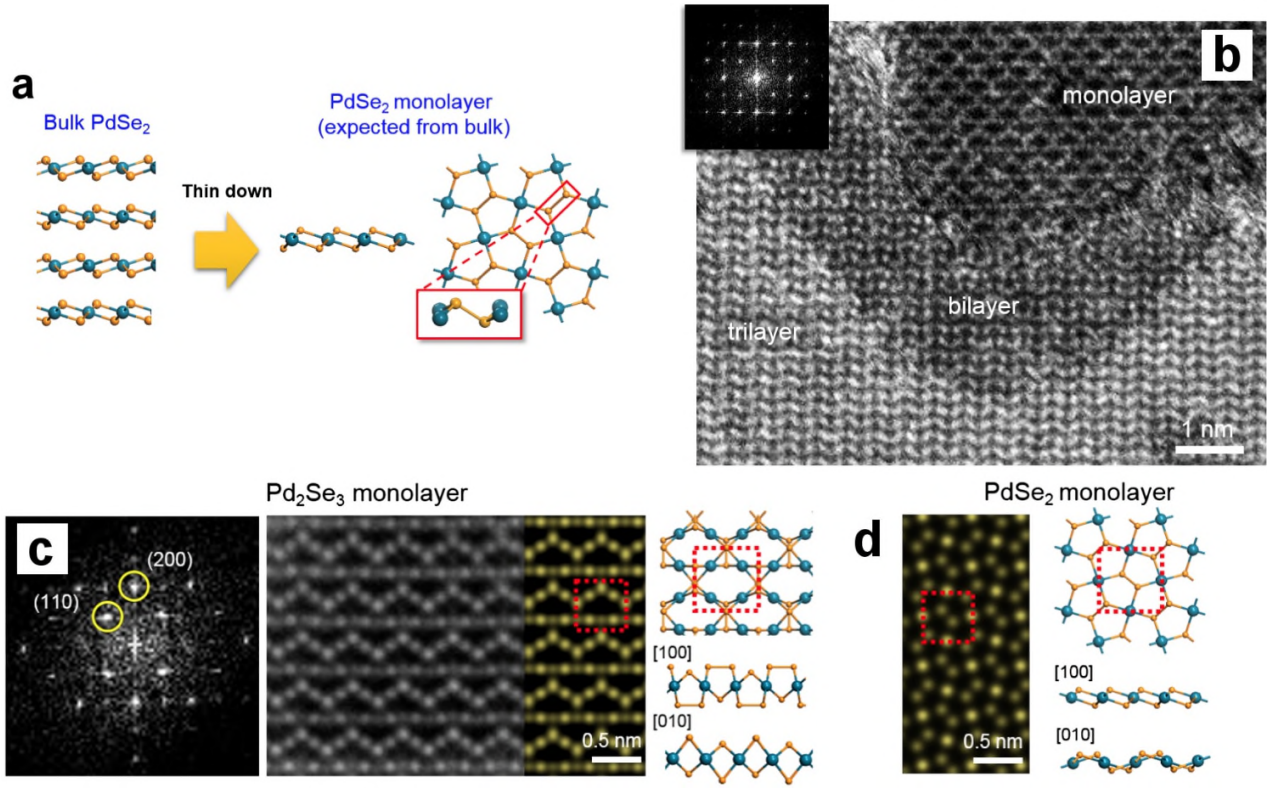

Figure 25. The formation of a Pd_2Se_3 monolayer by Se depletion from bilayer $PdSe_2$. (a) The bulk atomic structure of PdSe2 (cross section view), and the expected monolayer structure (top view). (b) ADF-STEM image showing trilayer, bilayer, and monolayer regions of a mechanically exfoliated $PdSe_2$ sample. The insert shows the FFT of the image. (c) A high-resolution view showing the atomic structure of the reconstructed Pd_2Se_3 monolayer, alongside a FFT, image simulation (yellow) and atomic models. (d) A simulated image and atomic models of the expected $PdSe_2$ monolayer. (a)-(d) are reproduced with permission from ref. [156] © 2017 American Physical Society.

6. MXenes

Two-dimensional metal carbides or nitrides, or MXenes, have shown promise for energy storage.[160,161] Single layer flakes of $Ti_3C_2T_x$, titanium carbide MXene, have been characterised by atomic resolution ADF-STEM.[162,163] Figure 26a shows a single Ti monovacancy (V_{Ti}) in the MXene monolayer, alongside

a DFT optimised model and image simulation. Interestingly, the formation of clusters of titanium vacancies was reported, such as the vacancy pair in Figure 26b. These vacancies can occur in any of the three metal sublayers of the MXene monolayer, and in the case of Figure 26c the contrast difference between the two vacancies suggests that they are in distinct layers. Interestingly, when the titanium vacancies occur in the same sublayer, as in Figure 26d and e, they form into a geometric honeycomb configuration. DFT calculations suggest a minimal energy cost to the system for coalescing these vacancies in this manner (Figure 26g), however getting reliable formation energies for larger vacancy clusters is limited by the size of the input repeat-unit super-cell and the resultant boundary interactions. It was then demonstrated that the Ti vacancies form due to HF solution treatment, and their concentration may be tuned altering the HF concentration.[163]

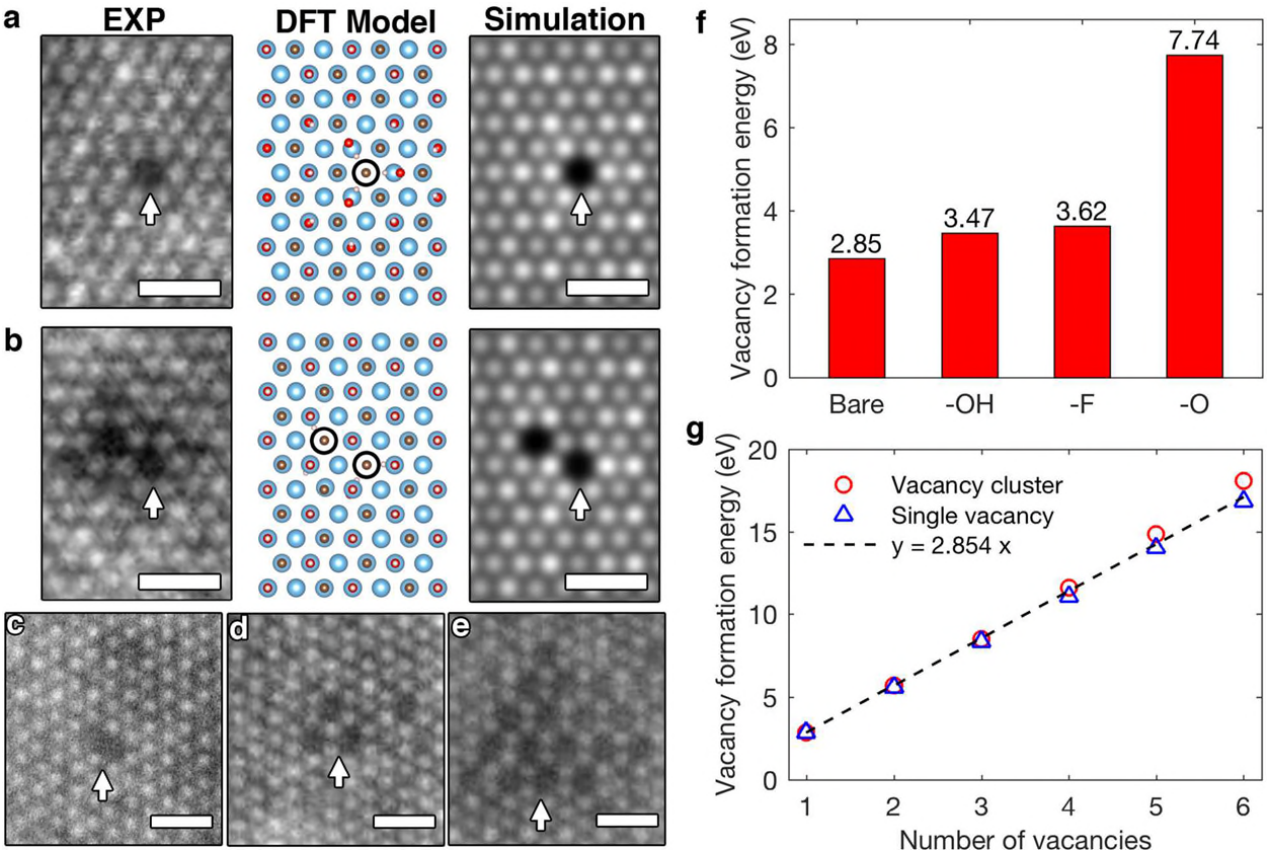

Figure 26. Defects in titanium carbide MXene monolayers. (a,b) HAADF-STEM image, DFT calculated structure, and image simulation, of a titanium vacancy V_{Ti} and two adjacent titanium vacancies, respectively. (c) Two adjacent V_{Ti} forming in adjacent metal sublayers. (d) Three V_{Ti} formed within the same sublayer, and (e) 17 V_{Ti} formed within the same sublayer, exhibiting a geometric arrangement. (f) DFT calculated formation energies for V_{Ti} depending on the termination of the Ti MXene. (g) Calculated formation energies for V_{Ti} clusters. (a)-(g) are reproduced with permission from ref. [163] © 2016 American Chemical Society.

Conclusion

AC-TEM and ADF-STEM are powerful tools that can resolve the atomic structure of a wide range of defects and dopants in monolayer materials. The high energy electron beam causes vacancy production at

nearly all energies and therefore care must be taken when considering the origin of vacancies and the effect of the electron beam on the sensitive structures. The three atom thick structure of many of the inorganic 2D materials gives rise to more complex 3D vacancy structures. The ability to integrate a wide range of elements into a single 2D material by alloying or substitutional doping provides greater means for tuning the band structure and properties of the 2D TMDs. The interaction of surface bound dopants with the underlying 2D substrate host is very sensitive to the presence of residual surface carbon and therefore it is important to be sure that the structures being examined are free from such interference when deducing the stable formed structures. The use of atomically resolved EELS was shown to be essential for correct identification of dopants and defects in 2D TMD systems, because HAADF contrast alone cannot give unambiguous outcomes. As more new 2D inorganic materials emerge, the role of atomic resolution characterization will continue to be critical to prove structure, deduce the defect forms, and to understand how these impact the electronic, chemical, optical and magnetic properties.

Acknowledgements

SW thanks the support from the China Scholarship Council. AR thanks the support from the Royal Society. JHW thanks the support from the Royal Society and the European Research Council (Grant No: 725 258).

References

1 M. Chhowalla, H. S. Shin, G. Eda, L.-J. Li, K. P. Loh and H. Zhang, *Nat. Chem.*, 2013, **5**, 263–275.

2 X. Duan, C. Wang, A. Pan, R. Yu and X. Duan, *Chem. Soc. Rev.*, 2015, **44**, 8859–8876.

3 S. Z. Butler, S. M. Hollen, L. Cao, Y. Cui, J. A. Gupta, H. R. Gutie´rrez, T. F. Heinz, S. S. Hong, J. Huang, A. F. Ismach, E. Johnston-Halperin, M. Kuno, V. V. Plashnitsa, R. D. Robinson, R. S. Ruoff, S. Salahuddin, J. Shan, L. Shi, M. G. Spencer, M. Terrones, W. Windl and J. E. Goldberge, *ACS Nano*, 2013, **7**, 2898–2926.

4 W. Choi, N. Choudhary, G. H. Han, J. Park, D. Akinwande and Y. H. Lee, *Mater. Today*, 2017, **20**, 116–130.

5 C. Ataca, H. Şahin and S. Ciraci, *J. Phys. Chem. C*, 2012, **116**, 8983–8999.

6 C. Ataca, M. Topsakal, E. Aktürk and S. Ciraci, *J. Phys. Chem. C*, 2011, **115**, 16354–16361.

7 F. A. Rasmussen and K. S. Thygesen, *J. Phys. Chem. C*, 2015, **119**, 13169–13183.

8 A. Molina-Sánchez and L. Wirtz, *Phys. Rev. B*, 2011, **84**, 155413.

9 A. Splendiani, L. Sun, Y. Zhang, T. Li, J. Kim, C.-Y. Chim, G. Galli and F. Wang, *Nano Lett.*, 2010, **10**, 1271–1275.

10 J. He, K. Hummer and C. Franchini, *Phys. Rev. B*, 2014, **89**, 075409.

11 J. Yan, J. Xia, X. Wang, L. Liu, J. L. Kuo, B. K. Tay, S. Chen, W. Zhou, Z. Liu and Z. X. Shen, *Nano Lett.*, 2015, **15**, 8155–8161.

12 K. Liu, L. Zhang, T. Cao, C. Jin, D. Qiu, Q. Zhou, A. Zettl, P. Yang, S. G. Louie and F. Wang, *Nat. Commun.*, 2014, **5**, 4966.

13 H. Li, Q. Zhang, C. C. R. Yap, B. K. Tay, T. H. T. Edwin, A. Olivier and D. Baillargeat, *Adv. Funct. Mater.*, 2012, **22**, 1385–1390.

14 A. Ramasubramaniam, D. Naveh and E. Towe, *Phys. Rev. B*, 2011, **84**, 205325.

15 Q. Liu, L. Li, Y. Li, Z. Gao, Z. Chen and J. Lu, *J. Phys. Chem. C*, 2012, **116**, 21556–21562.

16 T. Chu, H. Ilatikhameneh, G. Klimeck, R. Rahman and Z. Chen, *Nano Lett.*, 2015, **15**, 8000–8007.

17 Y. Yu, S. Y. Huang, Y. Li, S. N. Steinmann, W. Yang and L. Cao, *Nano Lett.*, 2014, **14**, 553–558.

18 W. Bao, X. Cai, D. Kim, K. Sridhara and M. S. Fuhrer, *Appl. Phys. Lett.*, 2013, **102**, 42104.

19 D. J. Late, Y. K. Huang, B. Liu, J. Acharya, S. N. Shirodkar, J. Luo, A. Yan, D. Charles, U. V. Waghmare, V. P. Dravid and C. N. R. Rao, *ACS Nano*, 2013, **7**, 4879–4891.

20 H. Li, Z. Yin, Q. He, H. Li, X. Huang, G. Lu, D. W. H. Fam, A. I. Y. Tok, Q. Zhang and H. Zhang, *Small*, 2012, **8**, 63–67.

21 J. R. Schaibley, H. Yu, G. Clark, P. Rivera, J. S. Ross, K. L. Seyler, W. Yao and X. Xu, *Nat. Rev. Mater.*, 2016, **1**, 16055.

22 R. Suzuki, M. Sakano, Y. J. Zhang, R. Akashi, D. Morikawa, A. Harasawa, K. Yaji, K. Kuroda, K. Miyamoto, T. Okuda, K. Ishizaka, R. Arita and Y. Iwasa, *Nat. Nanotechnol.*, 2014, **9**, 611–617.

23 J. Lee, K. F. Mak and J. Shan, *Nat. Nanotechnol.*, 2016, **11**, 421–425.

24 Q. Tang and D. Jiang, *ACS Catal.*, 2016, **6**, 4953–4961.

25 D. Wang, X. Zhang, S. Bao, Z. Zhang, H. Fei and Z. Wu, *J. Mater. Chem. A*, 2017, **5**, 2681–2688.

26 Y. Gong, J. Lin, X. Wang, G. Shi, S. Lei, Z. Lin, X. Zou, G. Ye, R. Vajtai, B. I. Yakobson, H. Terrones, M. Terrones, B. K. Tay, J. Lou, S. T. Pantelides, Z. Liu, W. Zhou and P. M. Ajayan, *Nat. Mater.*, 2014, **13**, 1135–1142.

27 J. M. Woods, Y. Jung, Y. Xie, W. Liu, Y. Liu, H. Wang and J. J. Cha, *ACS Nano*, 2016, **10**, 2004–2009.

28 R. Cheng, D. Li, H. Zhou, C. Wang, A. Yin, S. Jiang, Y. Liu, Y. Chen, Y. Huang and X. Duan, *Nano Lett.*, 2014, **14**, 5590–5597.

29 J. Kang, J. Li, S. Li, J. Xia and L. Wang, *Nano Lett.*, 2013, **13**, 5485–5490.

30 Y. Gong, S. Lei, G. Ye, B. Li, Y. He, K. Keyshar, X. Zhang, Q. Wang, J. Lou, Z. Liu, R. Vajtai, W. Zhou and P. M. Ajayan, *Nano Lett.*, 2015, **15**, 6135–6141.

31 H. Tan, W. Xu, Y. Sheng, C. S. Lau, Y. Fan, Q. Chen, M. Tweedie, X. Wang, Y. Zhou and J. H. Warner, *Adv. Mater.*, 2017, **29**, 1702917.

32 I. Song, C. Park and H. C. Choi, *RSC Adv.*, 2015, **5**, 7495–7514.

33 R. Ganatra and Q. Zhang, *ACS Nano*, 2014, **8**, 4074–4099.

34 Q. Ji, Y. Zhang, Y. Zhang and Z. Liu, *Chem. Soc. Rev.*, 2015, **44**, 2587-2602.

36 A. A. Tedstone, D. J. Lewis and P. O'Brien, *Chem. Mater.*, 2016, **28**, 1965–1974.

37 J. H. Warner, E. R. Margine, M. Mukai, A. W. Robertson, F. Giustino and A. I. Kirkland, *Science*, 2012, **337**, 209–212.

38 A. W. Robertson, K. He, A. I. Kirkland and J. H. Warner, *Nano Lett.*, 2014, **14**, 908–914.

39 K. He, G.-D. Lee, A. W. Robertson, E. Yoon and J. H. Warner, *Nat. Commun.*, 2014, **5**, 3040.

40 A. W. Robertson, C. S. Allen, Y. A. Wu, K. He, J. Olivier, J. Neethling, A. I. Kirkland and J. H. Warner, *Nat. Commun.*, 2012, **3**, 1144.

41 A. W. Robertson, B. Montanari, K. He, C. S. Allen, Y. a. Wu, N. M. Harrison, A. I. Kirkland and J. H. Warner, *ACS Nano*, 2013, **7**, 4495–4502.

42 C. Gong, A. W. Robertson, K. He, G. Lee, E. Yoon, C. S. Allen, A. I. Kirkland and J. H. Warner, *ACS Nano*, 2015, **9**, 10066–10075.

43 J. C. Meyer, C. Kisielowski, R. Erin, M. D. Rossell and M. F. Crommie, *Nano Lett.*, 2008, **8**, 3582–3586.

44 Z. Liu, K. Suenaga, P. J. F. Harris and S. Iijima, *Phys. Rev. Lett.*, 2009, **102**, 015501.

45 H.-P. Komsa, J. Kotakoski, S. Kurasch, O. Lehtinen, U. Kaiser and A. V. Krasheninnikov, *Phys. Rev. Lett.*, 2012, **109**, 035503.

46 R. Zan, Q. M. Ramasse, R. Jalil, T. Georgiou, U. Bangert and K. S. Novoselov, *ACS Nano*, 2013, **7**, 10167–10174.

47 O. L. Krivanek, M. F. Chisholm, V. Nicolosi, T. J. Pennycook, G. J. Corbin, N. Dellby, M. F. Murfitt, C. S. Own, Z. S. Szilagyi, M. P. Oxley, S. T. Pantelides and S. J. Pennycook, *Nature*, 2010, **464**, 571–574.

48 M. A. Py and R. R. Haering, *Can. J. Phys.*, 1983, **61**, 76–84.

49 Y.-C. Lin, D. O. Dumcenco, Y.-S. Huang and K. Suenaga, *Nat. Nanotechnol.*, 2014, **9**, 391–396.

50 S. Wang, H. Sawada, C. S. Allen, A. I. Kirkland and J. H. Warner, *Nanoscale*, 2017, **9**, 13060–13068.

51 A. Yan, W. Chen, C. Ophus, J. Ciston, Y. Lin, K. Persson and A. Zettl, *Phys. Rev. B*, 2016, **93**, 041420.

52 M.-Y. Li, Y. Shi, C.-C. Cheng, L.-S. Lu, Y.-C. Lin, H.-L. Tang, M.-L. Tsai, C.-W. Chu, K.-H. Wei, J.-H. He, W.-H. Chang, K. Suenaga and L.-J. Li, *Science*, 2015, **349**, 524–528.

53 J. Kotakoski, J. C. Meyer, S. Kurasch, U. Kaiser and A. V Krasheninnikov, *Phys. Rev. B*, 2011, **83**, 245420.

54 A. W. Robertson, G. Do Lee, K. He, E. Yoon, A. I. Kirkland and J. H. Warner, *Nano Lett.*, 2014, **14**, 1634–1642.

55 C. Gong, K. He, A. W. Robertson, E. Yoon, G. Lee and J. H. Warner, 2015, **9**, 656–662.

56 Y.-C. Lin, T. Bjorkman, H. Komsa, P. Teng, C. Yeh, F. Huang, Y. Lin and K. Suenaga, *Nat. Commun.*, 2015, **6**, 6736.

57 H.-P. Komsa, S. Kurasch, O. Lehtinen, U. Kaiser and A. V. Krasheninnikov, *Phys. Rev. B*, 2013, **88**, 035301.

58 W. Zhou, X. Zou, S. Najmaei, Z. Liu, Y. Shi, J. Kong, J. Lou, P. M. Ajayan, B. I. Yakobson and J.-C. Idrobo, *Nano Lett.*, 2013, **13**, 2615–2622.

59 S. Wang, H. Li, H. Sawada, C. S. Allen, A. I. Kirkland, J. C. Grossman and J. H. Warner, *Nanoscale*, 2017, **9**, 6417–6426.

60 S. Wang, G.-D. Lee, S. Lee, E. Yoon and J. H. Warner, *ACS Nano*, 2016, **10**, 5419–5430.

61 H. Liu, L. Jiao, F. Yang, Y. Cai, X. Wu, W. Ho, C. Gao, J. Jia, N. Wang, H. Fan, W. Yao and M. Xie, *Phys. Rev. Lett.*, 2014, **113**, 066105.

62 J. Lin, S. T. Pantelides and W. Zhou, *ACS Nano*, 2015, **9**, 5189–5197.

63 H. Y. Jeong, Y. Jin, S. J. Yun, J. Zhao, J. Baik, D. H. Keum, H. S. Lee and Y. H. Lee, *Adv. Mater.*, 2017, **29**, 1605043.

64 A. L. Koh, S. Wang, C. Ataca, J. C. Grossman, R. Sinclair and J. H. Warner, *Nano Lett.*, 2016, **16**, 1210–1217.

65 J. Lin, O. Cretu, W. Zhou, K. Suenaga, D. Prasai, K. I. Bolotin, N. T. Cuong, M. Otani, S. Okada, A. R. Lupini, J.-C. Idrobo, D. Caudel, A. Burger, N. J. Ghimire, J. Yan, D. G. Mandrus, S. J. Pennycook and S. T. Pantelides, *Nat. Nanotechnol.*, 2014, **9**, 436–442.

66 S. Wang, Z. Qin, G. S. Jung, F. J. Martin-Martinez, K. Zhang, M. J. Buehler and J. H. Warner, *ACS Nano*, 2016, **10**, 9831–9839.

67 S. Najmaei, Z. Liu, W. Zhou, X. Zou, G. Shi, S. Lei, B. I. Yakobson, J.-C. Idrobo, P. M. Ajayan and J. Lou, *Nat. Mater.*, 2013, **12**, 754–759.

68 A. Azizi, X. Zou, P. Ercius, Z. Zhang, A. L. Elías, N. Perea-López, G. Stone, M. Terrones, B. I. Yakobson and N. Alem, *Nat. Commun.*, 2014, **5**, 4867.

69 A. M. van der Zande, P. Y. Huang, D. A. Chenet, T. C. Berkelbach, Y. You, G.-H. Lee, T. F. Heinz, D. R. Reichman, D. A. Muller and J. C. Hone, *Nat. Mater.*, 2013, **12**, 554–561.

70 S. Zhou, S. Wang, H. Li, W. Xu, C. Gong, J. C. Grossman and J. H. Warner, *ACS Omega*, 2017, **2**, 3315–3324.

71 Q. Chen, H. Li, W. Xu, S. Wang, H. Sawada, C. S. Allen, A. I. Kirkland, J. C. Grossman and J. H. Warner, *Nano Lett.*, 2017, **17**, 5502–5507.

72 J. G. Song, G. H. Ryu, S. J. Lee, S. Sim, C. W. Lee, T. Choi, H. Jung, Y. Kim, Z. Lee, J. M. Myoung, C. Dussarrat, C. Lansalot-Matras, J. Park, H. Choi and H. Kim, *Nat. Commun.*, 2015, **6**, 1–10.

73 D. O. Dumcenco, H. Kobayashi, Z. Liu, Y.-S. Huang and K. Suenaga, *Nat. Commun.*, 2013, **4**, 1351.

74 H. Liu, K. K. A. Antwi, S. Chua and D. Chi, *Nanoscale*, 2014, **6**, 624–629.

75 Y. Chen, J. Xi, D. O. Dumcenco, Z. Liu, K. Suenaga, D. Wang, Z. Shuai, Y. S. Huang and L. Xie, *ACS Nano*, 2013, **7**, 4610–4616.

76 Z. Wang, P. Liu, Y. Ito, S. C. Ning, Y. W. Tan, T. Fujita, A. Hirata and M. W. Chen, *Sci. Rep.*, 2016, **6**, 21536.

77 Q. Feng, Y. Zhu, J. Hong, M. Zhang, W. Duan, N. Mao, J. Wu, H. Xu, F. Dong, F. Lin, C. Jin, C. Wang, J. Zhang and L. Xie, *Adv. Mater.*, 2014, **26**, 2648–2653.

78 Y. Gong, Z. Liu, A. R. Lupini, G. Shi, J. Lin, S. Najmaei, Z. Lin, A. L. Elías, A. Berkdemir, G. You, H. Terrones, M. Terrones, R. Vajtai, S. T. Pantelides, S. J. Pennycook, J. Lou, W. Zhou and P. M. Ajayan, *Nano Lett.*, 2014, **14**, 442–449.

79 Q. Fu, L. Yang, W. Wang, A. Han, J. Huang, P. Du and Z. Fan, *Adv. Mater.*, 2015, **2**, 4732–4738.

80 J. Lin, J. Zhou, S. Zuluaga, Y. Peng, M. Gu, Z. Liu, S. T. Pantelides and K. Suenaga, *ACS Nano*, 2018, **12**, 894–901.

81 K. Zhang, S. Feng, J. Wang, A. Azcatl, N. Lu, R. Addou, N. Wang, C. Zhou, J. Lerach, V. Bojan, M. J. Kim, L.-Q. Chen, R. M. Wallace, M. Terrones, J. Zhu and J. A. Robinson, *Nano Lett.*, 2015, **15**, 6586–6591.

82 Y. C. Lin, D. O. Dumcenco, H.-P. Komsa, Y. Niimi, A. V. Krasheninnikov, Y.-S. Huang and K. Suenaga, *Adv. Mater.*, 2014, **26**, 2857–2861.

83 J. Gao, Y. D. Kim, L. Liang, J. C. Idrobo, P. Chow, J. Tan, B. Li, L. Li, B. G. Sumpter, T. M. Lu, V. Meunier, J. Hone and N. Koratkar, *Adv. Mater.*, 2016, **28**, 9735–9743.

84 S. Sasaki, Y. Kobayashi, Z. Liu, K. Suenaga, Y. Maniwa, Y. Miyauchi and Y. Miyata, *Appl. Phys. Express*, 2016, **9**, 71201.

85 A. W. Robertson, Y. Lin, S. Wang, H. Sawada, C. S. Allen, Q. Chen, S. Lee, G. Lee, S. Han, E. Yoon, A. I. Kirkland, H. Kim, K. Suenaga and J. H. Warner, *ACS Nano*, 2016, **10**, 10227–10236.

86 Y. C. Lin, S. Li, H. P. Komsa, L. J. Chang, A. V. Krasheninnikov, G. Eda and K. Suenaga, *Adv. Funct. Mater.*, 2018, **28**, 1704210.

87 Y. Sheng, X. Wang, K. Fujisawa, S. Ying, A. L. Elias, Z. Lin, W. Xu, Y. Zhou, A. M. Korsunsky, H. Bhaskaran, M. Terrones and J. H. Warner, *ACS Appl. Mater. Interfaces*, 2017, **9**, 15005–15014.

88 H. Li, S. Wang, T. Samuels, G. Ggoch, D. Han, C. S. Allen, A. I. Kirkland, J. C. Grossman and H. Jamie, *ACS Nano*, 2017, **11**, 3392–3403.

89 G. Liu, A. W. Robertson, M. M.-J. Li, W. C. H. Kuo, M. T. Darby, M. H. Muhieddine, Y.-C. Lin, K. Suenaga, M. Stamatakis, J. H. Warner and S. C. E. Tsang, *Nat. Chem.*, 2017, **9**, 810–816.

90 J. Hong, Y. Pan, Z. Hu, D. Lv, C. Jin, W. Ji, J. Yuan and Z. Zhang, *Nano Lett.*, 2017, **17**, 3383–3390.

91 S. Wang, H. Sawada, Q. Chen, G. G. D. Han, C. Allen, A. I. Kirkland and J. H. Warner, *ACS Nano*, 2017, **11**, 9057–9067.

92 S. Wang, H. Li, J. Zhang, S. Guo, W. Xu, J. C. Grossman and J. H. Warner, *ACS Nano*, 2017, **11**, 6404–6415.

93 B. E. Brown, *Acta Crystallogr.*, 1966, **20**, 268–274.

94 I. Pletikosić, M. N. Ali, A. V. Fedorov, R. J. Cava and T. Valla, *Phys. Rev. Lett.*, 2014, **113**, 216601.

95 M. N. Ali, J. Xiong, S. Flynn, J. Tao, Q. D. Gibson, L. M. Schoop, T. Liang, N. Haldolaarachchige, M. Hirschberger, N. P. Ong and R. J. Cava, *Nature*, 2014, **514**, 205–208.

96 S. Tang, C. Zhang, Di. Wong, Z. Pedramrazi, H. Z. Tsai, C. Jia, B. Moritz, M. Claassen, H. Ryu, S. Kahn, J. Jiang, H. Yan, M. Hashimoto, D. Lu, R. G. Moore, C. C. Hwang, C. Hwang, Z. Hussain, Y. Chen, M. M. Ugeda, Z. Liu, X. Xie, T. P. Devereaux, M. F. Crommie, S. K. Mo and Z. X. Shen, *Nat. Phys.*, 2017, **13**, 683–687.

97 F. Zheng, C. Cai, S. Ge, X. Zhang, X. Liu, H. Lu, Y. Zhang, J. Qiu, T. Taniguchi, K. Watanabe, S. Jia, J. Qi, J. H. Chen, D. Sun and J. Feng, *Adv. Mater.*, 2016, **28**, 4845–4851.

98 X. Qian, J. Liu, L. Fu and J. Li, *Science*, 2014, **346**, 1344–1347.

99 Y. Wang, J. Xiao, H. Zhu, Y. Li, Y. Alsaid, K. Y. Fong, Y. Zhou, S. Wang, W. Shi, Y. Wang, A. Zettl, E. J. Reed and X. Zhang, *Nature*, 2017, **550**, 487–491.

100 D. H. Keum, S. Cho, J. H. Kim, D. H. Choe, H. J. Sung, M. Kan, H. Kang, J. Y. Hwang, S. W. Kim, H. Yang, K. J. Chang and Y. H. Lee, *Nat. Phys.*, 2015, **11**, 482–486.

101 C. H. Naylor, W. M. Parkin, J. Ping, Z. Gao, Y. R. Zhou, Y. Kim, F. Streller, R. W. Carpick, A. M. Rappe, M. Drndić, J. M. Kikkawa and A. T. C. Johnson, *Nano Lett.*, 2016, **16**, 4297–4304.

102 C. H. Naylor, W. M. Parkin, Z. Gao, H. Kang, M. Noyan, R. B. Wexler, L. Z. Tan, Y. Kim, C. E. Kehayias, F. Streller, Y. R. Zhou, R. Carpick, Z. Luo, Y. W. Park, A. M. Rappe, M. Drndić, J. M. Kikkawa and A. T. C. Johnson, *2D Mater.*, 2017, **4**, 21008.

103 N. Lu, C. Zhang, C.-H. Lee, J. P. Oviedo, M. A. T. Nguyen, X. Peng, R. M. Wallace, T. E. Mallouk, J. A. Robinson, J. Wang, K. Cho and M. J. Kim, *J. Phys. Chem. C*, 2016, **120**, 8364–8369.

104 M. Kan, J. Y. Wang, X. W. Li, S. H. Zhang, Y. W. Li, Y. Kawazoe, Q. Sun and P. Jena, *J. Phys. Chem. C*, 2014, **118**, 1515–1522.

105 H.-J. Lamfers, A. Meetsma, G. A. Wiegers and J. L. de Boer, *J. Alloys Compd.*, 1996, **241**, 34–39.

106 S. Tongay, H. Sahin, C. Ko, A. Luce, W. Fan, K. Liu, J. Zhou, Y.-S. Huang, C.-H. Ho, J. Yan, D. F. Ogletree, S. Aloni, J. Ji, S. Li, J. Li, F. M. Peeters and J. Wu, *Nat. Commun.*, 2014, **5**, 3252.

107 F. Liu, S. Zheng, X. He, A. Chaturvedi, J. He, W. L. Chow, T. R. Mion, X. Wang, J. Zhou, Q. Fu, H. J. Fan, B. K. Tay, L. Song, R. H. He, C. Kloc, P. M. Ajayan and Z. Liu, *Adv. Funct. Mater.*, 2016, **26**, 1169–1177.

108 E. Zhang, Y. Jin, X. Yuan, W. Wang, C. Zhang, L. Tang, S. Liu, P. Zhou, W. Hu and F. Xiu, *Adv. Funct. Mater.*, 2015, **25**, 4076–4082.

109 Y. C. Lin, H. P. Komsa, C. H. Yeh, T. Björkman, Z. Y. Liang, C. H. Ho, Y. S. Huang, P. W. Chiu, A. V. Krasheninnikov and K. Suenaga, *ACS Nano*, 2015, **9**, 11249–11257.

110 K. Wu, B. Chen, S. Yang, G. Wang, W. Kong, H. Cai, T. Aoki, E. Soignard, X. Marie, A. Yano, A. Suslu, B. Urbaszek and S. Tongay, *Nano Lett.*, 2016, **16**, 5888–5894.

111 W. Wen, J. Lin, K. Suenaga, Y. Guo, Y. Zhu, H.-P. Hsu and L. Xie, *Nanoscale*, 2017, **9**, 18275–18280.

112 J. A. Wilson, F. J. Di Salvo and S. Mahajan, *Adv. Phys.*, 1975, **24**, 117–201.

113 K. Rossnagel, *J. Phys.: Condens. Matter*, 2011, **23**, 213001.

114 R. Hovden, A. W. Tsen, P. Liu, B. H. Savitzky, I. El Baggari, Y. Liu, W. Lu, Y. Sun, P. Kim, A. N. Pasupathy and L. F. Kourkoutis, *Proc. Natl. Acad. Sci.*, 2016, **113**, 11420–11424.

115 R. Samnakay, D. Wickramaratne, T. R. Pope, R. K. Lake, T. T. Salguero and A. A. Balandin, *Nano Lett.*, 2015, **15**, 2965–2973.

116 A. M. Gabovich, A. I. Voitenko, J. F. Annett and M. Ausloos, *Supercond. Sci. Technol.*, 2001, **14**, R1–R27.

117 V. G. Tissen, M. R. Osorio, J. P. Brison, N. M. Nemes, M. García-Hernández, L. Cario, P. Rodière, S. Vieira and H. Suderow, *Phys. Rev. B*, 2013, **87**, 134502.

118 F. Güller, C. Helman and A. M. Llois, in *Physica B,* 2012*,* **407**, 3188–3191.

119 X. Wang, J. Lin, Y. Zhu, C. Luo, K. Suenaga, C. Cai and L. Xie, *Nanoscale*, 2017, **9**, 16607–16611.

120 E. Navarro-Moratalla, J. O. Island, S. Manãs-Valero, E. Pinilla-Cienfuegos, A. Castellanos-Gomez, J. Quereda, G. Rubio-Bollinger, L. Chirolli, J. A. Silva-Guillén, N. Agraït, G. A. Steele, F. Guinea, H. S. J. Van Der Zant and E. Coronado, *Nat. Commun.*, 2016, **7**, 11043.

121 Y. Yu, F. Yang, X. F. Lu, Y. J. Yan, Y. H. Cho, L. Ma, X. Niu, S. Kim, Y. W. Son, D. Feng, S. Li, S. W. Cheong, X. H. Chen and Y. Zhang, *Nat. Nanotechnol.*, 2015, **10**, 270–276.

122 X. Xi, L. Zhao, Z. Wang, H. Berger, L. Forró, J. Shan and K. F. Mak, *Nat. Nanotechnol.*, 2015, **10**, 765–769.

123 C. J. Arguello, S. P. Chockalingam, E. P. Rosenthal, L. Zhao, C. Gutiérrez, J. H. Kang, W. C. Chung, R. M. Fernandes, S. Jia, A. J. Millis, R. J. Cava and A. N. Pasupathy, *Phys. Rev. B*, 2014, **89**, 235115.

124 L. Nguyen, H. P. Komsa, E. Khestanova, R. J. Kashtiban, J. J. P. Peters, S. Lawlor, A. M. Sanchez, J. Sloan, R. V. Gorbachev, I. V. Grigorieva, A. V. Krasheninnikov and S. J. Haigh, *ACS Nano*, 2017, **11**, 2894–2904.

125 M. J. Hÿtch, J. L. Putaux and J. M. Pénisson, *Nature*, 2003, **423**, 270–273.

126 M. J. Hÿtch, E. Snoeck and R. Kilaas, *Ultramicroscopy*, 1998, **74**, 131–146.

127 H. Wang, X. Huang, J. Lin, J. Cui, Y. Chen, C. Zhu, F. Liu, Q. Zeng, J. Zhou, P. Yu, X. Wang, H. He, S. H. Tsang, W. Gao, K. Suenaga, F. Ma, C. Yang, L. Lu, T. Yu, E. H. T. Teo, G. Liu and Z. Liu, *Nat. Commun.*, 2017, **8**, 394.

128 G. Algara-siller, S. Kurasch, M. Sedighi, O. Lehtinen and U. Kaiser, *Appl. Phys. Lett.*, 2013, **103**, 203107.

129 A. W. Robertson, A. Bachmatiuk, Y. a. Wu, F. Schäffel, B. Rellinghaus, B. Büchner, M. H. Rümmeli and J. H. Warner, *ACS Nano*, 2011, **5**, 6610–6618.

130 A. W. Robertson, G. Do Lee, K. He, E. Yoon, A. I. Kirkland and J. H. Warner, *Nano Lett.*, 2014, **14**, 3972–3980.

131 E. Cockayne, G. M. Rutter, N. P. Guisinger, J. N. Crain, P. N. First and J. A. Stroscio, *Phys. Rev. B*, 2011, **83**, 195425.

132 O. V. Yazyev and Y. P. Chen, *Nat. Nanotechnol.*, 2014, **9**, 755–767.

133 J. Bennetto, J. W. Nunes and D. Vanderbilt, *Phys. Rev. Lett.*, 1997, **79**, 245–248.

134 X. Zou, Y. Liu and B. I. Yakobson, *Nano Lett.*, 2013, **13**, 253–258.

135 R. F. Egerton, P. Li and M. Malac, *Micron*, 2004, **35**, 399–409.

136 J. C. Meyer, F. Eder, S. Kurasch, V. Skakalova, J. Kotakoski, H. J. Park, S. Roth, A. Chuvilin, S. Eyhusen, G. Benner, A. V. Krasheninnikov and U. Kaiser, *Phys. Rev. Lett.*, 2012, **108**, 196102.

137 W. A. McKinley and H. Feshbach, *Phys. Rev.*, 1948, **74**, 1759–1763.

138 F. Banhart, J. Kotakoski and A. V. Krasheninnikov, *ACS Nano*, 2011, **5**, 26–41.

139 F. Banhart, *Reports Prog. Phys.*, 1999, **62**, 1181–1221.

140 L. Sun, F. Banhart and J. Warner, *MRS Bull.*, 2015, **40**, 29–37.

141 R. F. Egerton, R. McLeod, F. Wang and M. Malac, *Ultramicroscopy*, 2010, **110**, 991–997.

142 P. A. Thrower and R. M. Mayer, *Phys. status solidi*, 1978, **47**, 11–37.

143 J. Dai and X. C. Zeng, *Angew.Chem. Int. Ed.*, 2015, **54**, 7572–7576.

144 J. O. Island, M. Barawi, R. Biele, A. Almazán, J. M. Clamagirand, J. R. Ares, C. Sánchez, H. S. J. van der Zant, J. V Álvarez, R. D'Agosta, I. J. Ferrer and A. Castellanos-Gomez, *Adv. Mater.*, 2015, **27**, 2595–2601.

145 R. B. Jacobs-Gedrim, M. Shanmugam, N. Jain, C. A. Durcan, M. T. Murphy, T. M. Murray, R. J. Matyi, R. L. Moore and B. Yu, *ACS Nano*, 2014, **8**, 514–521.

146 H. Zhang, X. Zhang, C. Liu, S. T. Lee and J. Jie, *ACS Nano*, 2016, **10**, 5113–5122.

147 K. He, Y. Zhang, K. He, C. Chang, C. Song, L. Wang, X. Chen, J. Jia, Z. Fang, X. Dai, W. Shan, S. Shen, Q. Niu, X. Qi, S. Zhang, X.-C. Ma and Q.-K. Xue, *Nat. Phys.*, 2010, **6**, 584–588.

148 D. Kong, W. Dang, J. J. Cha, H. Li, S. Meister, H. Peng, Z. Liu and Y. Cui, *Nano Lett.*, 2010, **10**, 2245–2250.

149 X. Zhang and Y. Xie, *Chem. Soc. Rev.*, 2013, **42**, 8187.

150 Z. Wang, K. Xu, Y. Li, X. Zhan, M. Safdar, Q. Wang, F. Wang and J. He, *ACS Nano*, 2014, **8**, 4859–4865.

151 S. Urazhdin, D. Bilc, S. H. Tessmer, S. D. Mahanti, T. Kyratsi and M. G. Kanatzidis, *Phys. Rev. B*, 2002, **66**, 161306.

152 T. Topological, B. Te, Y. L. Chen, J. G. Analytis, J.-H. Chu, Z. K. Liu, S.-K. Mo, X. L. Qi, H. J. Zhang, D. H. Lu, X. Dai, Z. Fang, S. C. Zhang, I. R. Fisher, Z. Hussain and Z.-X. Shen, *Science*, 2009, **325**, 178–181.

153 M. Lin, D. Wu, Y. Zhou, W. Huang, W. Jiang, W. Zheng, S. Zhao, C. Jin, Y. Guo, H. Peng and Z. Liu, *J. Am. Chem. Soc.*, 2013, **135**, 13274–13277.

154 J. Jasinski, W. Swider, J. Washburn, Z. Liliental-Weber, A. Chaiken, K. Nauka, G. A. Gibson and C. C. Yang, *Appl. Phys. Lett.*, 2002, **81**, 4356–4358.

155 J. Zhou, Q. Zeng, D. Lv, L. Sun, L. Niu, W. Fu, F. Liu, Z. Shen, C. Jin and Z. Liu, *Nano Lett.*, 2015, **15**, 6400–6405.

156 J. Lin, S. Zuluaga, P. Yu, Z. Liu, S. T. Pantelides and K. Suenaga, *Phys. Rev. Lett.*, 2017, **119**, 016101.

157 P. Mirõ, M. Ghorbani-Asl and T. Heine, *Angew.Chem. Int. Ed.*, 2014, **53**, 3015–3018.

158 J. Sun, H. Shi, T. Siegrist and D. J. Singh, *Appl. Phys. Lett.*, 2015, **107**, 153902.

159 P. Miró, M. Audiffred and T. Heine, *Chem. Soc. Rev.*, 2014, **43**, 6537–6554.

160 M. Ghidiu, M. R. Lukatskaya, M. Q. Zhao, Y. Gogotsi and M. W. Barsoum, *Nature*, 2015, **516**, 78–81.

161 M. R. Lukatskaya, O. Mashtalir, C. E. Ren, Y. D. Agnese, M. W. Barsoum and Y. Gogotsi, *Science*, 2013, **341**, 1502–1506.

162 L. H. Karlsson, J. Birch, J. Halim, M. W. Barsoum and P. O. Å. Persson, *Nano Lett.*, 2015, **15**, 4955–4960.

163 X. Sang, Y. Xie, M. W. Lin, M. Alhabeb, K. L. Van Aken, Y. Gogotsi, P. R. C. Kent, K. Xiao and R. R. Unocic, *ACS Nano*, 2016, **10**, 9193–9200.